Molecular Cancer

RESEARCH

Open Access

# IGF2BP3 promotes progression of head and neck cancers through the circHECTD2/hsa_miR_4310/7157-5p/Smad2 signaling axis in an m$^6$A modification–dependent manner

Kainan Wu[1,2,3†], Fen Chang[1,2†], Tianjian Peng[1,2], Siyu Wang[1,2], Xiangkai Sun[1,2], Yin Wang[1,2], Zinan Li[1,2], Chengcheng Duan[1,2], Jingao Li[1,2], Yijing Zhang[1,2], Tongdong Su[1,2], Wenming Li[1,2], Dongmin Wei[1,2], Shengda Cao[1,2], Jun Liu[4,5], Jugao Fang[6], Long Chen[1,2], Guojun Li[7], Neil Gross[7], Juan Zhao[1,2] and Dapeng Lei[1,2,3*]

## Abstract

**Background** Accumulating evidence indicates that N6-methyladenosine (m$^6$A) modification of circular RNAs (circRNAs) plays a pivotal role in regulating cancer progression. However, in head and neck squamous cell carcinoma (HNSCC), the biological functions and underlying mechanisms of m$^6$A modification in circRNAs remain insufficiently elucidated.

**Methods** In this study, we analyzed the association between the expression of IGF2BP3—an upstream m$^6$A reader—and clinical outcomes of HNSCC patients, followed by investigating the interaction between IGF2BP3 and circHECTD2 as well as the effect of m$^6$A modification on this interaction. Additionally, we explored the molecular mechanism by which IGF2BP3 and circHECTD2 regulate HNSCC progression, focusing on their roles in modulating microRNAs (miRNAs) and target mRNAs, and validated the functional impacts of the IGF2BP3/circHECTD2 axis on HNSCC cell proliferation, invasion, and metastasis.

**Results** We found high expression of the m$^6$A reader IGF2BP3 was significantly associated with poor clinical outcomes in HNSCC patients. Further experiments showed that IGF2BP3 directly bound to circHECTD2 and stabilized it, and m$^6$A modification of circHECTD2 enhanced this binding and stabilization effect. Mechanistically, circHECTD2 functioned as a competing endogenous RNA (ceRNA) to sponge hsa-miR-4310 and hsa-miR-7157-5p, thereby preventing the miRNA-mediated degradation of SMAD2 mRNA. Ultimately, the IGF2BP3/circHECTD2/SMAD2 axis was shown to promote HNSCC cell proliferation, invasion, and metastasis.

**Conclusion** We delineate an m$^6$A-dependent IGF2BP3/circHECTD2/SMAD2 regulatory axis that contributes to HNSCC malignancy. Elevated IGF2BP3 expression correlates with poor patient outcome and enhances circHECTD2 stability through m6A-facilitated binding; circHECTD2 in turn acts as a ceRNA to sequester hsa-miR-4310 and hsa-miR-

†Kainan Wu and Fen Chang contributed equally to this work.

*Correspondence:
Dapeng Lei
leidapeng@sdu.edu.cn

Full list of author information is available at the end of the article

7157-5p, thereby maintaining SMAD2 expression. Functionally, this axis promotes HNSCC cell proliferation, invasion and metastasis. Collectively, these findings suggest that IGF2BP3 and circHECTD2 may serve as promising prognostic biomarkers and therapeutic targets for HNSCC.

**Keywords** IGF2BP3, CircHECTD2, N6-methyladenosine, SMAD2, HNSCC

## Introduction

Head and neck squamous cell carcinoma (HNSCC) refers to a group of malignant tumors originating from the mucosal epithelium of the oral cavity, pharynx, and larynx and ranks as the seventh most common cancer globally [1]. HNSCC is associated with a poor prognosis, a high tendency for local invasion and lymphatic metastasis, and frequent infiltration of critical structures [2]. Despite advancements in treatment modalities, the 5-year survival rate remains dismally low, at less than 50% [3]. Projections from the Global Cancer Observatory suggest a 60% increase in incidence by 2025 [4]. Therefore, exploring novel biomarkers and molecular mechanisms of HNSCC with the aim of prolonging patient survival is of significant clinical importance.

Circular RNAs (circRNAs) are a class of single-stranded, closed circle-shaped RNAs generated through back-splicing [5]. circRNAs are more stable than their linear counterpart [6]. circRNAs participate in various physiological and pathological processes, including tumorigenesis and cancer progression, via multiple mechanisms, including transcriptional regulation; alternative splicing; acting as molecular sponges for microRNAs (miRNAs) [7]; interacting with functional proteins; and even undergoing translation [8]. The tissue-specific expression of circRNAs and their stable detectability in liquid biopsy samples (e.g., plasma, saliva, and urine) highlight their potential as promising biomarkers for early cancer diagnosis and prognostication [9–11]. Our research group and others have demonstrated that circRNAs are closely associated with poor prognosis in HNSCC, suggesting their potential as therapeutic targets and biomarkers [12–14].

RNA methylation is a major form of RNA epigenetic modification, accounting for over 60% of total RNA modifications, and N6-methyladenosine ($m^6A$) modification is the most prevalent type of RNA methylation [15]. $m^6A$ modification is a dynamic and reversible process regulated by methyltransferases ("writers") [16], demethylases ("erasers") [17], and $m^6A$-binding proteins ("readers") that recognize and mediate the effects of $m^6A$ modification [18–20]. In cancer, $m^6A$ modification influences proliferation, metabolism, and metastasis by regulating various biological processes, including RNA splicing, degradation, and translation [21–23]. Reports indicate that RNA $m^6A$ modification can regulate HNSCC progression; for example, Huang et al. demonstrated that $m^6A$ modification promotes the maturation and accumulation of miR-151-5p, a process regulated by methyltransferase-like 3 (METTL3). miR-151-5p directly targets LY6/PLAUR domain-containing 3 (LYPD3) by binding to the 3'-untranslated region of *LYPD3* mRNA through complementary base pairing, thereby accelerating HNSCC metastasis [24]. Zhao et al. confirmed that $m^6A$-modified *HOXA10-AS* and its downstream miR-29b-3p/ITGA6 axis regulate oxidative resistance and malignant progression of laryngeal SCC (LSCC) through the Notch and Keap1/Nrf2 pathways, suggesting that targeting this axis may represent a potential therapeutic strategy for LSCC [25]. Additionally, studies have shown that activation of the TMA7-UBA2-PI3K pathway, regulated by the $m^6A$ methylation reader IGF2BP3, is the main mechanism by which TMA7 inhibits autophagy and promotes LSCC progression [26]. However, the relationship between $m^6A$ modification of non-coding RNAs (especially circRNAs) and HNSCC, as well as the underlying molecular mechanisms, remains to be fully elucidated.

In this study, we identified distinct $m^6A$ modification profiles of circRNAs in HNSCC and adjacent non-tumor tissues. Our findings demonstrate that the $m^6A$ reader IGF2BP3 is significantly upregulated in HNSCC tissues and that IGF2BP3 upregulation strongly correlates with poor clinical prognosis. Furthermore, we identified circHECTD2 as a downstream target of IGF2BP3. IGF2BP3 binds to the GG($m^6A$)C motif within circHECTD2, thereby stabilizing circHECTD2 and enhancing its capacity to adsorb downstream miRNAs miR-4310 and miR-7157-5p. This interaction reduces the degradation of *SMAD2* mRNA by miR-4310 and miR-7157-5p, consequently driving HNSCC progression. Our findings suggest that IGF2BP3 and circHECTD2 may serve as potential prognostic biomarkers and therapeutic targets for HNSCC.

## Methods

### Patient specimens

HNSCC tissues and matched adjacent non-tumor tissues were collected from patients who underwent resection at Qilu Hospital of Shandong University (Shandong, China). All specimens were independently identified by three pathologists, and the collection of human specimens was approved by the Ethics Committee of Qilu Hospital of Shandong University (KYLL-2020(KS)-320). The inclusion criteria for HNSCC patients were (1) HNSCC confirmed by pathology; (2) new cases with no

treatment before surgery; and (3) patients gave written informed consent. The exclusion criteria were (1) subtype on pathological examination adenocarcinoma, malignant melanoma, malignant lymphoma, soft tissue sarcoma, or other non-squamous cell carcinoma; (2) HNSCC present in combination with other subtype; (3) patient had other acquired or congenital immunodeficiency disease, e.g., severe liver, kidney, or other systemic disease, or a history of organ transplant; and (4) patients received preoperative chemotherapy or radiotherapy. All samples were stored at -80 °C until use. Detailed clinicopathological characteristics are provided in Supplementary Table 1.

#### Cell lines and cell cultures

Human HNSCC cell lines, including FaDu, Tu686, and SCC9, were obtained from the American Type Culture Collection. FaDu and Tu686 cells were cultured in Dulbecco's modified Eagle medium (DMEM; Gibco, Grand Island, NY, USA), and SCC9 cells were maintained in DMEM/F12 medium (HyClone, USA). Both types of media were supplemented with 10% fetal bovine serum (Gibco), 100 U/mL penicillin, and 100 μg/mL streptomycin (HyClone). All cells were incubated in a humidified atmosphere containing 5% $CO_2$ at 37 °C.

#### Transfection of small interfering RNA (siRNA) and establishment of stably transfected cell lines

For overexpression experiments, the coding DNA sequence regions of *IGF2BP3* and *SMAD2* were cloned into the pLenti-C-Myc-DDK-IRES-Puro plasmid vector (Origene, Catalog No. PS100069). The empty pLenti-C-Myc-DDK-IRES-Puro vector served as the negative control.

For gene knockdown experiments, two small interfering RNAs (siRNAs) each were designed for IGF2BP3, circHECTD2, and SMAD2, respectively, to minimize off-target effects, and all siRNAs were purchased from Sangon Biotech Co., Ltd. The knockdown efficiency was verified using reverse transcription-quantitative polymerase chain reaction (qRT-PCR) and Western blotting. Corresponding primers targeting common sequences of si-IGF2BP3-1/2, si-circHECTD2-1/2, and si-SMAD2-1/2 were annealed and cloned into the pLKO.1–TRC plasmid vector (Addgene, Catalog No. 10878) to construct the knockdown plasmids shIGF2BP3-1/2, shcircHECTD2-1/2, and shSMAD2-1/2.

siRNA transfection: HNSCC cell lines were seeded into six-well plates 24 h prior to transfection. When cell confluence reached 50% to 70%, transfection was performed using jetPRIME transfection reagent (Polyplus Transfection, Illkirch, France) following the manufacturer's protocol.

Establishment of stably transfected cell lines: shRNAs were co-transfected with packaging system psPAX2/pMD2.G (Addgene, #12260/ #12259) into HEK-293T cells. Cells were adjusted to optimal density before transfection. At 48 h after transfection, the supernatant containing lentivirus was collected, centrifuged, filtered, and ultracentrifuged for virus concentration. The concentrated virus was aliquoted and stored at -80 °C. HNSCC cells were infected with the lentivirus; this was followed by medium replacement and selection with puromycin. The knockdown efficiency was confirmed by qRT-PCR and Western blotting.

The pLC5-ciR and pLC5-ciR-circHECTD2 plasmids were purchased from GRNESEED (GS0108). miRNA overexpression plasmids were purchased form GenePharma. The pmirGLO plasmid was purchased from Promega. All target sequences are listed in Supplementary Table 2.

#### qRT-PCR

For qRT-PCR, total RNA was isolated from tissues or cells using TRIzol reagent (Invitrogen) following the manufacturer's instructions. RNA was reverse-transcribed into cDNA using PrimeScript RT Master Mix (Takara, Japan). Real-time PCR was performed with the SYBR Premix Ex Taq kit (Takara, Japan) and specific primers (Supplementary Table 2) on the StepOnePlus real-time PCR system (Applied Biosystems, USA). Actin beta was used as the endogenous reference gene, and the relative expression levels of target genes were calculated using the $2^{(-\Delta\Delta CT)}$ method.

#### Western blotting

Proteins were extracted using RIPA Lysis Buffer (Thermo Fisher Scientific, USA), and protein concentration was determined by the BCA method. Equal amounts of proteins from cell lysates were separated by using 4% to 20% SDS-PAGE gels (Bio-Rad) and electrotransferred onto nitrocellulose membranes (GE Healthcare). Membranes were blocked with 5% skim milk powder at 37 °C for 30 min, incubated with primary antibodies (diluted 1:1000 according to the manufacturer's instructions) at 4 °C overnight, and then incubated with secondary antibodies at room temperature for 1 h. Finally, protein bands were visualized using the Odyssey CLx Imaging System.

#### CCK-8, colony formation, Transwell, scratch wound healing, and EdU incorporation assays

CCK-8 assay: Cell viability was assessed using the Cell Counting Kit-8 (CCK-8, Dojindo, Tokyo, Japan). Plasmid-transfected cells were seeded into 96-well plates at a density of 10,000 cells per well and cultured for 0, 24, 48, 72, and 96 h, respectively. A 10-μL volume of CCK-8 solution was added to each well, and then cells were incubated at 37 °C for 2 h. The optical density value of each well was measured at 450 nm using a microplate reader

(Bio-Rad). The assay was performed with 3 independent biological experiments, and each condition included 6 technical replicate wells.

Colony formation assay: For colony formation assays, 200 to 400 cells were seeded into 6-cm-diameter dishes. After 10 to 14 days of culture, cells were fixed with 4% paraformaldehyde (Beyotime) and stained with 0.1% crystal violet (Beyotime).

Transwell assay: Migration and invasion assays were performed using Transwell chambers (Corning, USA) with 8-μm-pore filters following the manufacturer's protocol. For the migration assays, cells were plated in the upper chambers ($5 \times 10^4$ cells/well) with 300 μL of serum-free medium, and the bottom chambers were filled with 600 μL of medium supplemented with 30% fetal bovine serum. After 24 h of incubation, non-migrated cells on the upper surface of the filters were gently removed with a cotton swab. Cells that had migrated to the lower surface were fixed with 4% paraformaldehyde for 10 min and stained with 0.5% crystal violet solution (Beyotime) for 30 min at room temperature. Finally, migrated cells were photographed and counted under a light microscope. For the invasion assays, the procedures were the same as for the migration assays except that the upper chambers were coated with Matrigel (C0371, Beyotime) at 37 °C before the cells were seeded.

Scratch wound healing assay: HNSCC cell lines were seeded into six-well plates. Once cells were confluent, a sterile 200-μL pipette tip was used to create uniform scratches in the cell monolayer, and the cells were then cultured in serum-free medium containing 1 μg/mL mitomycin. At 0, 12, and 24 h, images of the wounds were captured, and the wound width was measured.

5-Ethynyl-2'-deoxyuridine (EdU) incorporation assay: EdU incorporation assays were performed using the EdU cell proliferation kit (Beyotime, China). Briefly, cells were incubated with 10-μM EdU for 2 h, fixed with 4% paraformaldehyde, and permeabilized with 0.3% Triton X-100 for 15 min. Subsequently, cells were stained with click reaction buffer containing Azide 555 for 30 min and DAPI for 10 min. Images were acquired using the Lionheart FX Intelligent Cell Imaging Analysis System (BioTek, USA).

#### Nuclear-cytoplasmic fractionation

Nuclear and cytoplasmic RNAs were isolated from FaDu cells using Nuclear/Cytoplasmic Isolation Reagent (Thermo Fisher Scientific, USA) according to the manufacturer's protocol. Expression levels were normalized to Hsp90 (cytoplasmic control) and PCNA (nuclear control), and relative quantification was performed using the $2^{(-\Delta\Delta CT)}$ method.

#### RNase R and actinomycin D treatment

Total RNA (1 μg) was treated with or without 2 U/μg RNase R (Abcam) at 37 °C for 15 min. Additionally, FaDu cells were treated with actinomycin D (1 μg/mL; Abcam) for 0, 4, 8, 12, and 24 h. Quantitative real-time PCR (qRT-PCR) was subsequently performed for detection.

#### RNA fluorescence in situ hybridization (FISH)

For FISH, circRNA or miRNA was hybridized with Cy3-labeled or FITC-labeled probes following the manufacturer's protocols (RiboBio, China). Nuclei were stained with DAPI. The localization of circRNA or miRNA in HNSCC cell lines was observed using a confocal laser scanning microscope (Olympus FV1000).

#### Immunohistochemistry (IHC) and immunofluorescence analyses

For IHC analyses, paraffin sections were incubated with the primary antibody against IGF2BP3 (ab179807; dilution 1:300). Staining was scored on the basis of two parameters: intensity of positive staining (strong = 3, moderate = 2, weak = 1, negative = 0) and percentage of positively stained cells (> 75% = 4, 51%–75% = 3, 26%–50% = 2, ≤ 25% = 1). Images were captured using an Olympus multifunctional microscope (Olympus BX51, Tokyo, Japan). All evaluations were conducted independently by three senior pathologists using the same microscope.

For immunofluorescence experiments, hypopharyngeal carcinoma tissue sections were dehydrated and incubated with anti-IGF2BP3 antibody (ab177477; dilution 1:300) at 4 °C overnight. After washing, sections were incubated with the fluorescent secondary antibody (Alexa Fluor 488-conjugated goat anti-rabbit IgG; Thermo Fisher Scientific) and imaged using a fluorescence microscope (DM5000B, Leica).

#### Electrophoretic mobility shift assay (EMSA)

Biotin-labeled RNA probes were synthesized by Sangon Biotech. EMSA was performed using the LightShift Chemiluminescent RNA EMSA Kit (Thermo Fisher Scientific, Waltham, USA, #20158) following the manufacturer's instructions.

#### Northern blotting

Northern blotting was performed using the DIG Northern Starter Kit (12039672910, Roche) with minor modifications to the manufacturer's protocol. DNA templates for in vitro synthesis of digoxigenin-labeled probes (targeting circHECTD2 or linear *HECTD2* mRNA) were generated by PCR with the primer sequences listed in Supplementary Table 2. Ten micrograms of total RNA (with or without RNase R digestion) was resolved on 2% agarose gels containing formaldehyde and then

transferred to a Hybond-N+ membrane (Solarbio) via capillary transfer. RNA was crosslinked to the membrane by UV irradiation (200,000 mJ/cm² at 265 nm). Hybridization was carried out at 68 °C for 6 h using a biotin-labeled oligonucleotide probe. Membranes were blocked in blocking buffer for 30 min and then incubated in antibody solution for 30 min with gentle shaking. After three washes with washing buffer, membranes were incubated in detection solution for 5 min and exposed to X-ray film. GAPDH served as the internal control.

#### RNA in situ hybridization (RNA-ISH)

RNA-ISH was performed using a digoxin-labeled probe specific for circHECTD2 to assess circHECTD2 expression in tissue samples from Qilu Hospital. The tissue sections were dewaxed and rehydrated and then digested with proteinase K. Hybridization with the digoxin-labeled probe specific for circHECTD2 was carried out at 45 °C overnight. Subsequently, the sections were incubated with biotin-conjugated anti-digoxin antibodies at 4 °C overnight and stained with 3,3'-diaminobenzidine. Samples were categorized into low or high expression groups based on the mean RNA-ISH scores.

#### RNA immunoprecipitation (RIP) and m$^6$A methylated RIP (MeRIP)

RIP assays were performed using the RNA Immunoprecipitation Kit (Geneseed, China) following the manufacturer's instructions. Briefly, cells were lysed in 1×Buffer A supplemented with 1% protease inhibitor and RNase inhibitor. For each reaction, 100 μL of Protein A + G beads were pretreated with 0.5 mL of 1×Buffer A and 10 μL of Buffer D at 4 °C for 30 min, then washed twice with 1×Buffer A. The pretreated beads were resuspended in 1 mL of 1×Buffer A and incubated with 5 μg of anti-PURB, anti–Argonaute 2, or IgG antibodies at 4 °C for 2 h. After two washes with 1×Buffer A, the antibody-bead complexes were incubated with cell lysates at 4 °C overnight and then washed five times with 1×Buffer B (2 min each with vortexing). Immunoprecipitated RNAs were extracted, reverse-transcribed, and detected by qRT-PCR.

m$^6$A MeRIP assays were performed using the m$^6$A MeRIP Kit (BersinBio™, China). Total cellular RNA was extracted and quality-checked, then fragmented by ultrasonic treatment. A 50-μL aliquot was retained as the input group, and the remaining RNA was divided into two 400-μL aliquots, labeled the IP and IgG groups. For the IP group, 20 μL of IP buffer 2 and 4 μg of anti-m$^6$A antibody were added; for the IgG group, 20 μL of IP buffer 2 and 4 μg of IgG antibody were added. Both groups were incubated at 4 °C for 4 h on a vertical mixer. For magnetic bead preparation, 40 μL of Protein A + G magnetic beads were mixed with 500 μL of IP buffer 3, then placed on a magnetic rack to collect beads and remove supernatant. Beads were resuspended in 360 μL of IP buffer 3 with 40 μL of BSA, shaken at 4 °C for 2 h, and then washed twice with 200 μL of IP buffer 3. Beads were resuspended in 200 μL of IP buffer 3 and split into two 100-μL aliquots, which were added to the IP and IgG groups, respectively. The mixtures were then incubated at 4 °C for 1 h on a vertical mixer. Beads were collected on a magnetic rack, and supernatants were discarded. Both groups were washed three times with 500 μL of IP buffer 3 (5 min each at 4 °C on a vertical mixer). RNA was eluted by incubating beads with 200 μL of Elution Buffer and 2 μL of Proteinase K at 4 °C with vertical mixing. After beads were collected on a magnetic rack, supernatants were transferred to RNase-free tubes. Immunoprecipitated RNAs were extracted, reverse-transcribed, and detected by qRT-PCR.

#### m6A RNA-Seq and data analysis

m6A RNA immunoprecipitation was performed with the GenSeqTM m6A RNA IP Kit (GenSeq Inc., China) by following the manufacturer's instructions. Both the input sample without immunoprecipitation and the m6A IP samples were used for RNA-seq library generation with NEBNext® Ultra II Directional RNA Library Prep Kit (New England Biolabs, Inc., USA). The library quality was evaluated with BioAnalyzer 2100 system (Agilent Technologies, Inc., USA). Library sequencing was performed on an illumina Hiseq instrument with 150 bp paired-end reads.

Briefly, Paired-end reads were harvested from Illumina NovaSeq 6000 sequencer, and were quality controlled by Q30. After 3' adaptor-trimming and low quality reads removing by cutadapt software (v1.9.3). First, clean reads of input libraries were aligned to reference genome (UCSC HG19) by STAR software. Then circRNAs were identified by DCC software using the STAR alignment results. After that, clean reads of all libraries were aligned to the reference genome by Hisat2 software (v2.0.4). Methylated sites on RNAs (peaks) were identified by MACS software. Differentially methylated sites were identified by diffReps. These peaks identified by both softwares overlapping with exons of mRNA, LncRNA and circRNA were figured out and choosed by homemade scripts. GO and Pathway enrichment analysis were performed by the differentially methylated protein coding genes, the associated genes of differentially methylated LncRNAs and the source genes of differentially methylated circRNAs separately.

#### CircRNA-seq and data analysis

Ribosomal RNA (rRNA) was removed from the samples using the NEBNext rRNA Depletion Kit (New England Biolabs, Inc., Massachusetts, USA). The sequencing

library was constructed with the NEBNext® Ultra™ II Directional RNA Library Prep Kit (New England Biolabs, Inc., Massachusetts, USA). Library quality control and quantification were performed using the BioAnalyzer 2100 system (Agilent Technologies, USA), followed by 150 bp paired-end sequencing on the Illumina NovaSeq 6000 platform.

After sequencing on the Illumina NovaSeq 6000 instrument, paired-end reads were generated. Quality control was conducted based on Q30 scores, and adapter sequences and low-quality reads were trimmed using Cutadapt software (v1.9.3) to obtain high-quality reads. These high-quality reads were aligned to the reference genome/transcriptome using STAR software (v2.5.1b), and circular RNAs (circRNAs) were detected and identified with DCC software (v0.4.4).

The identified circRNAs were annotated using the circBase database and Circ2Traits. Subsequently, data normalization and screening of differentially expressed circRNAs were performed using edgeR software (v3.16.5). Additionally, Gene Ontology (GO) and Kyoto Encyclopedia of Genes and Genomes (KEGG) pathway analyses were conducted for the host genes of the differentially expressed circRNAs.

#### RNA antisense purification

Biotin-labeled probes targeting the junction site of circHECTD2 were synthesized by Sangon Biotech. RNA antisense purification was performed using the RNA Antisense Purification Kit (Bes5103-3, BersinBio) following the manufacturer's instructions. Potential interacting proteins were subsequently analyzed by Western blotting.

#### RNA pull-down

Biotin-labeled circHECTD2 oligonucleotide probes (Sangon Biotech) were incubated with BeyoMagM streptavidin magnetic beads (Beyotime; P2151) at room temperature for 60 min. After binding to streptavidin magnetic beads, the complexes were incubated overnight at 4 °C with whole-cell lysates supplemented with protease/phosphatase inhibitor cocktail and RNase inhibitor. Following washes with ice-cold PBS, RNA complexes bound to the beads were eluted, extracted using the RNeasy Mini Kit (QIAGEN), and analyzed by qRT-PCR. For protein detection, the RNA-protein binding mixture was boiled in SDS buffer, and the eluted proteins were analyzed by Western blotting.

#### Dual-luciferase reporter assay

After complete lysis of cells, the supernatant was collected by centrifugation for subsequent assays. For luciferase activity detection, luciferase assay working solution was prepared by adding luciferase assay substrate (100×) to luciferase assay buffer at a ratio of 1:100 and adjusting the total volume according to the requirement of 100 μL per sample. For each sample, 20 μL to 100 μL of cell lysate was taken, and an equal volume of reporter cell lysate was used as the blank control. Then, 100 μL of firefly luciferase detection reagent was added, the mixture was mixed thoroughly, and the relative light unit (RLU) value was measured using a microplate reader (Bio-Rad). For Renilla luciferase detection, 100 μL of Renilla luciferase working solution was added, the mixture was mixed thoroughly, and the RLU value was measured similarly. The firefly luciferase RLU value was normalized to the Renilla luciferase RLU value for final analysis.

#### Protein–nucleic acid docking

Sequence information of target proteins and nucleic acids has been provided. Protein and nucleic acid structure prediction based on sequence using alphafold3. The two proteins were interfaced using the professional HDOCKv1.1 tool. The empirical iterated scoring function ITScorePP was used to score molecular docking and configuration. A negative score indicates molecular binding. The greater the absolute value, the stronger the binding ability. The maximum output configuration quantity color was set to 100, and the top 10 configurations were scored. The configuration with the highest docking score was selected for subsequent analysis, and PyMOL was used for 3D mapping analysis. LigPlot software was used to analyze residues that interacted between proteins.

In this study, the tool HDOCK was used for molecular docking, and a total of 100 binding configurations were generated. The docking scores of the top 10 configurations were calculated. The docking score given by HDOCK can reflect the tightness of the bond to some extent but is only a preliminary estimate of affinity. Amore accurate prediction of binding free energy requires molecular dynamics simulation to obtain specific data, and the final experimental data shall be subject to.

#### Xenograft models

Female BALB/c nude mice (4–6 weeks old, weighing 18–22 g) were purchased from Beijing Vital River. All animal care and experimental procedures were conducted in accordance with the guidelines of the Animal Care and Use Committee and approved by Qilu Hospital of Shandong University (KYLL-2023(ZM)-150). The nude mice were housed in a barrier environment in strict accordance with "Laboratory Animal Requirements of Environment and Facilities". Specific conditions were as follows: temperature was controlled at 22 ± 2 °C, humidity at 50 ± 5%, with a 12-hour light/12-hour dark cycle; the housing density per cage complied

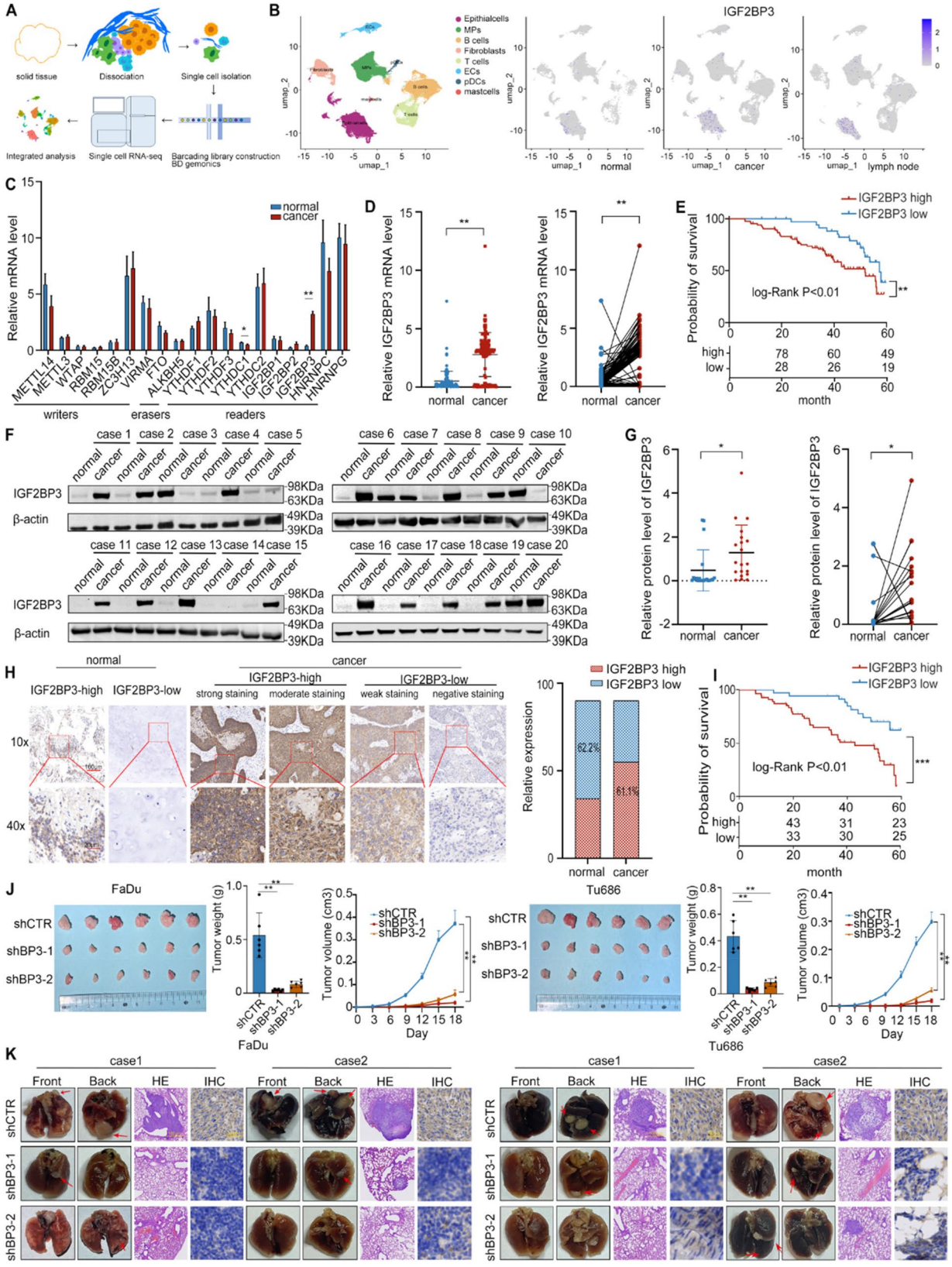


**Fig. 1** (See legend on next page.)

(See figure on previous page.)

**Fig. 1** Increased IGF2BP3 Expression Correlates with Poor Prognosis and Drives HNSCC Progression In Vivo and In Vitro. (**A**) Flow chart of single-cell RNA sequencing. (**B**) Uniform manifold approximation and projection plot showing the different cell subsets. The feature plot demonstrates the expression levels of *IGF2BP3* in HNSCC tissues, adjacent non-tumor tissues, and metastatic lymph node tissues. (**C**) Expression levels of 19 common $m^6A$ modification-related genes in HNSCC tissues and adjacent non-tumor tissues by qPCR ($n=40$). Due to the non-normal distribution of the data, statistical analysis was performed using the Mann-Whitney U test. (**D**) Expression of *IGF2BP3* in HNSCC tissues and adjacent non-tumor tissues by qPCR ($n=120$). Due to the non-normal distribution of the data, statistical analysis was performed using the Mann-Whitney U test. (**E**) Survival curves of patients stratified by high and low IGF2BP3 expression in qRT-PCR experiments were analyzed using the Kaplan-Meier method with the log-rank test. (**F–G**) Western blot analysis of IGF2BP3 expression in 20 pairs of HNSCC tissues and matched adjacent non-tumor tissues. (**H**) IHC results of IGF2BP3 expression in 90 pairs of HNSCC tissues and adjacent non-tumor tissues. (**I**) Survival curves of patients stratified by high and low IGF2BP3 expression in IHC experiments were analyzed using the Kaplan-Meier method with the log-rank test. (**J**) FaDu and Tu686 cells of shIGF2BP3-1/2 and control groups were injected subcutaneously into the armpit of nude mice. Tumor volume was measured every three days, and growth curves were plotted. On the 19th day, the mice were killed, and tumors were excised and weighed ($n=6$). (**K**) Results of tumor dissection, hematoxylin-eosin (HE) staining, and IHC staining in nude mice with lung metastasis established by tail vein injection of IGF2BP3 knockdown and control FaDu and Tu686 cells. (**A-K**) Cancer: HNSCC tissues, normal: adjacent non-tumor tissues. Data are presented as mean ± SD, $^*p<0.05$, $^{**}p<0.01$, $^{***}p<0.001$ using Student's t test. BP3: IGF2BP3

with relevant standards, and standard sterile feed and sterilized drinking water were provided. Pollution and stress were strictly controlled to ensure animal welfare and the reliability of experimental results.

For the subcutaneous tumor model, 100 μL of cell suspension ($1\times10^7$ cells/mL) was subcutaneously injected into the axillary region of each mouse. Tumor volume was measured every three days using the formula $\text{volume} = \left(\text{length}\times\text{width}^2\right)/2$. After three weeks, the tumors were excised for further analysis.

For the metastatic tumor model, FaDu and Tu686 cells transfected with plasmids (shCTR, shIGF2BP3-1/2, shcircHECTD2-1/2, or shSMAD2-1/2) were injected into the tail veins of mice at a density of $1\times10^6$ cells per mouse. After six weeks, all mice were euthanized, and dissections were performed to examine metastases.

### Statistical analysis

Quantitative data were statistically analyzed using SPSS software (Chicago, IL, USA) and GraphPad Prism 5.0 software (GraphPad, San Diego, CA, USA). Experimental data are presented as the mean ± standard deviation from at least three independent experiments, each performed in triplicate. Prior to statistical analysis, normality tests (Shapiro-Wilk test) were conducted for all quantitative data. Student's t-test was used to analyze significant differences between groups for data that conformed to the normal distribution, while the Mann-Whitney U test was applied for data that failed the normality test. The chi-square test was used for comparisons of categorical data between groups. Overall survival curves were generated using the Kaplan-Meier method, and the log-rank test was applied to determine the significance of differences in overall survival curves. Spearman's correlation analysis was used to assess relationships between variables. $p<0.05$ was considered statistically significant.

## Results

### Increased IGF2BP3 expression correlates with poor prognosis and drives HNSCC progression in vivo and in vitro

To identify $m^6A$-related proteins that regulate methylation, we analyzed HNSCC transcriptome data from the Cancer Genome Atlas database. For 19 common key genes involved in $m^6A$ modification—including well-known "writers", "erasers", and "readers"—we generated heatmaps (Supplementary Fig. 1A), boxplots (Supplementary Fig. 1B), volcano plots (Supplementary Fig. 1C), and patient survival curves based on gene expression levels (Supplementary Fig. 1D, Supplementary Fig. 2) to compare gene expression between HNSCC tissues and adjacent non-tumor tissues. Results showed that *IGF2BP1* and *IGF2BP3* were differentially upregulated in tumor tissues, and patients with high expression of these genes had significantly poorer survival outcomes ($P<0.05$).

Given that transcriptome sequencing fails to exclude interference from other components in the tissues, we performed single-cell RNA sequencing (Fig. 1A) on five matched pairs of HNSCC tissues, adjacent non-tumor tissues, and metastatic lymph node tissues [27]. In these tissues, we analyzed expression of the 19 genes, generating dimensionality reduction clustering plots (Fig. 1B, Supplementary Fig. 3), bar charts of cellular proportion (Supplementary Fig. 1E), and volcano plots (Supplementary Fig. 1F–G). Results demonstrated that the expression of *IGF2BP3* increased in both HNSCC tissues and metastatic lymph node tissues compared with non-tumor tissues.

Both Cancer Genome Atlas data and single-cell RNA sequencing data indicated that *IGF2BP3* is upregulated in tumor tissues, suggesting it may be a key gene affecting methylation modification in HNSCC. We then detected the expression of the 19 genes in 40 pairs of HNSCC tissues and adjacent non-tumor tissues using qRT-PCR. Results showed that *IGF2BP3* mRNA expression was significantly upregulated in HNSCC tissues compared with adjacent tissues ($p<0.01$) (Fig. 1C). To validate

this finding, we analyzed *IGF2BP3* mRNA levels in 120 pairs of HNSCC tissues and adjacent tissues, confirming *IGF2BP3* upregulation in tumor tissues (Fig. 1D). Similarly, Western blot analysis of 20 pairs of matched HNSCC and adjacent non-tumor tissues showed increased IGF2BP3 protein levels in tumor tissues (Fig. 1F–G). IHC analysis of tissue microarrays containing 90 pairs of HNSCC tissues and adjacent non-tumor tissues further confirmed these results, with IGF2BP3 expression significantly higher in HNSCC tissues than in non-tumor tissues (Fig. 1H). We further analyzed the relationship between IGF2BP3 mRNA levels and clinicopathological characteristics in 120 HNSCC patients. Results showed that high *IGF2BP3* expression was significantly associated with tumor size and alcohol consumption (Table 1). Importantly, elevated IGF2BP3 expression was significantly associated with poor clinical outcomes in HNSCC patients (Fig. 1E and I).

To verify the role of IGF2BP3 in HNSCC, we first detected IGF2BP3 expression levels in various HNSCC cell lines. Among three common cell lines tested, FaDu and Tu686 cells exhibited relatively high expression of IGF2BP3, while SCC9 cells exhibited lower expression. On the basis of these findings, we established stable *IGF2BP3*-knockdown cell lines (shIGF2BP3-1/2) in FaDu and Tu686 cells and stable *IGF2BP3*-overexpressing cell lines in SCC9 cells (Supplementary Fig. 1H) for subsequent functional experiments. A series of functional assays—including CCK-8 (Supplementary Fig. 1I), EdU incorporation (Supplementary Fig. 1J), colony formation (Supplementary Fig. 1K), Transwell (Supplementary Fig. 1L), and scratch wound healing assays (Supplementary Fig. 1M)—were performed to evaluate the effects of IGF2BP3 knockdown. Results showed that *IGF2BP3* knockdown inhibited the proliferation, migration, and invasion abilities of FaDu and Tu686 cells. Conversely, in SCC9 cells, overexpression of *IGF2BP3* enhanced these abilities (Supplementary Fig. 4A–D). In vivo, nude mice were subcutaneously implanted with FaDu and Tu686 cells featuring stable IGF2BP3 knockdown, as well as SCC9 cells with stable IGF2BP3 overexpression, to establish xenograft models. Compared with the control group, the IGF2BP3 knockdown group exhibited a significant reduction in tumor weight and volume (Fig. 1J), while the overexpression group showed a marked increase in these parameters (Supplementary Fig. 4E). Additionally, *IGF2BP3*-knockdown FaDu and Tu686 cells were injected into the tail vein of nude mice to assess tumor cell capacity for formation of lung metastases. Subsequent hematoxylin-eosin and IHC staining of lung metastatic tumors showed that both metastatic potential and IGF2BP3 expression were lower in the knockdown group than in the control group (Fig. 1K). Statistical data on metastatic lung nodules are provided in Supplementary Fig. 5. These results demonstrated that IGF2BP3 overexpression enhances cell proliferation, invasion, and migration abilities, whereas *IGF2BP3* knockdown exerts the opposite effects, both in vitro and in vivo.

**Table 1** The relationship between IGF2BP3 expression and clinicopathological characteristics of 120 patients with HNSCC

| Characteristics | Total 120 | IGF2BP3 expression | | $\chi^2$ | *P* Value |
|---|---|---|---|---|---|
| | | High | Low | | |
| Age(y) | | | | 1.032 | 0.3097 |
| >=60 | 73 | 53 | 20 | | |
| <60 | 47 | 30 | 17 | | |
| Gender | | | | 3.803 | 0.0512 |
| Male | 114 | 81 | 33 | | |
| Female | 6 | 2 | 4 | | |
| Drink | | | | 50,542 | 0.0186 |
| No | 21 | 10 | 11 | | |
| Yes | 99 | 73 | 26 | | |
| T classification | | | | 8.657 | 0.0342 |
| T1 | 27 | 15 | 12 | | |
| T2 | 50 | 32 | 18 | | |
| T3 | 34 | 27 | 7 | | |
| T4 | 9 | 9 | 0 | | |
| N classification | | | | 5.75 | 0.1244 |
| N0 | 37 | 24 | 13 | | |
| N1 | 33 | 19 | 14 | | |
| N2 | 47 | 37 | 10 | | |
| N3 | 3 | 3 | 0 | | |
| Tumor differentiation | | | | 1.617 | 0.4455 |
| Well | 24 | 15 | 9 | | |
| Moderate | 67 | 49 | 18 | | |
| Poor | 29 | 18 | 11 | | |
| AJCC stage | | | | 2.186 | 0.5347 |
| I | 11 | 6 | 5 | | |
| II | 18 | 11 | 7 | | |
| III | 31 | 22 | 9 | | |
| IV | 60 | 44 | 16 | | |

### IGF2BP3 regulates novel circRNA circHECTD2 in HNSCC

To investigate the molecular mechanism by which IGF2BP3 regulates carcinogenic functions in HNSCC, we performed circRNA-seq and m$^6$A-circRNA-seq (MeRIP-circRNA-seq) in *IGF2BP3*-knockdown cells. Heatmaps of the top 20 upregulated and downregulated circRNAs, along with corresponding volcano plots, are presented for circRNA-seq (Fig. 2A–B) and methylated RNA immunoprecipitation sequencing (MeRIP-seq) (Fig. 2C–D). To identify downstream circRNAs regulated by IGF2BP3, we intersected the circRNA-seq and MeRIP-circRNA-seq datasets, which yielded three candidate circRNAs (Fig. 2E). Detailed information on these circRNAs is provided in Table 2. To identify the most relevant of these circRNAs, we validated their expression in control and *IGF2BP3*-knockdown cells. Results indicated

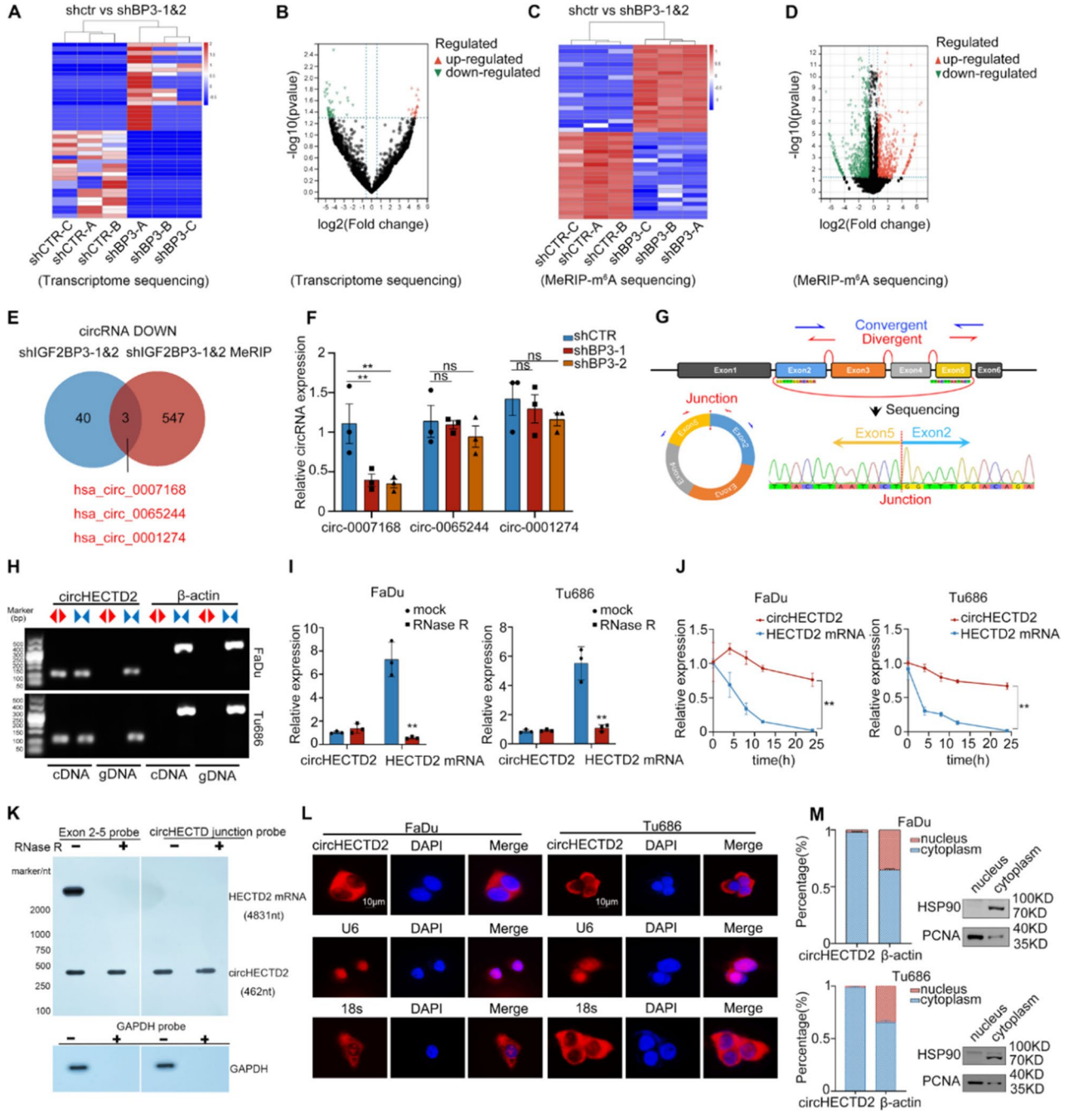


**Fig. 2** Identification and characterization of circHECTD2. (**A**) Heat map of top 20 upregulated and downregulated genes in terms of circRNA-seq. (**B**) Volcano plot of all genes in terms of circRNA-seq. (**C**) Heat map of top 20 upregulated and down-regulated genes in terms of MeRIP-circRNA-seq. (**D**) Volcano plot of all genes in terms of MeRIP-circRNA-seq. (**E**) Three candidate circRNAs discovered by intersection of circRNA-seq and MeRIP circRNA-seq datasets. Detailed information on the three candidate circRNAs is provided in Table 2. (**F**) qPCR results regarding expression of three candidate circRNAs in shIGF2BP3-1/2 and control cells. (**G**) Model diagram of circHECTD2. (**H**) Presence of circRNAs derived from the *HECTD2* gene validated by RT-PCR. Divergent primers amplified circRNAs in cDNA but not in genomic DNA. β-actin was used as a negative control. (**I**) qPCR to verify the effect of adding RNase R on the expression of *circHECTD2* and *HECTD2* mRNA. (**J**) qPCR to verify the effect of adding actinomycin D on the expression of *circHECTD2* and *HECTD2* mRNA at 0, 4, 8, 12, and 24 h. (**K**) Northern blot analysis of *circHECTD2* and *HECTD2* mRNA levels in FaDu cells by hybridization with exon 2–5 and junction probes with or without RNase R treatment. GAPDH mRNA with or without RNase R treatment was detected as a control. (**L**) FISH analysis of subcellular localization of circHECTD2 in FaDu and Tu686 cells. (**M**) Levels of circHECTD2 in the nuclear and cytoplasmic fractions of FaDu and Tu686 cells. HSP90 and PCNA were detected as a protein control. (A-M) BP3: IGF2BP3. Data are presented as mean ± SD, $^{**}p < 0.01$, ns, not significant, using Student's t test

**Table 2** circRNAs revealed by circBase and circInteractome

| circRNA ID | Location | Genomic Length (bp) | Spliced Length (bp) | RNAseq resources |
|---|---|---|---|---|
| hsa_circ_0007168 | chr10:93185037–93,221,941 | 36,904 | 462 | Salzman2013 (PMID:24039610) |
| hsa_circ_00065244 | Chr3:47651555–47,719,801 | 68,246 | 1536 | Salzman2013 (PMID: 24039610) |
| hsa_circ_0001274 | chr10:17051165–17,056,403 | 5238 | 2601 | Salzman2013 (PMID: 24039610) |

that circHECTD2, designated as hsa_circ_0007168 in circBase (http://www.circbase.org/), was most likely regulated by IGF2BP3 via m$^6$A modification (Fig. 2F). circHECTD2 is predicted to originate from head-to-tail splicing of exons 2, 3, 4, and 5 (462 bp) of the *HECTD2* gene (Fig. 2G). To exclude the possibility of trans-splicing or genomic rearrangement contributing to this head-to-tail splicing, we performed four validation steps. First, we designed convergent primers to amplify linear *HECTD2* mRNA and divergent primers to amplify circ0007168, using cDNA and gDNA from FaDu and Tu686 cells as templates. The results demonstrated that the divergent primers amplified circHECTD2 only from cDNA, not from gDNA (Fig. 2H). Second, we performed RNase R digestion analysis, which showed that circHECTD2 was resistant to RNase R digestion, whereas linear RNA was significantly degraded (Fig. 2I). Third, we treated cells with actinomycin D, which inhibits transcription, and found that circHECTD2 exhibited greater stability than linear *HECTD2* mRNA (Fig. 2J). Finally, we used probes hybridizing with the back-splice junction and exons 2–5 to distinguish circHECTD2 from its linear counterpart (Fig. 2K). To determine the subcellular localization of circHECTD2, we performed FISH assays for subcellular localization, which demonstrated that circHECTD2 was primarily cytoplasmic (Fig. 2L, Supplementary Fig. 6A), which was confirmed by nuclear-cytoplasmic fractionation analysis (Fig. 2M).

To verify whether IGF2BP3 regulates circHECTD2 expression, we assessed circHECTD2 levels in FaDu and Tu686 cells with modulated IGF2BP3 via qRT-PCR. Results showed that IGF2BP3 positively regulated circHECTD2 expression (Fig. 3A –B), while circHECTD2 had no effect on *IGF2BP3* mRNA levels (Supplementary Fig. 6B). To rule out the regulatory effect of IGF2BP3 on HECTD2 mRNA, we performed qRT-PCR experiments, which revealed that IGF2BP3 had no impact on HECTD2 mRNA expression (Supplementary Fig. 6C). After actinomycin D treatment, the degradation rate of circHECTD2 was slowed in *IGF2BP3*-knockdown cells (Fig. 3C). At the tissue level, ISH and IHC on serial sections showed expert-graded positive correlation between IGF2BP3 and circHECTD2 expression (Fig. 3D), confirmed by Spearman correlation analysis (Fig. 3E). Notably, patients with high co-expression of both IGF2BP3 and circHECTD2 had the poorest prognosis (Fig. 3F), and chi-square tests confirmed a significant association between their expression levels (Fig. 3G). For the qRT-PCR results of IGF2BP3 and circHECTD2 in tissue samples, we performed statistical analyses including Spearman correlation analysis, survival analysis based on expression level stratification, and chi-square test (Supplementary Fig. 6D). The results showed that the expression of IGF2BP3 was significantly positively correlated with that of circHECTD2, and patients with high expression of both molecules had the poorest prognosis. To determine if regulation involves interaction, we established a stable circHECTD2-overexpressing cell line (pLC5-circHECTD2) and performed RNA anti-sense purification (RAP) assays using a circHECTD2-specific probe in both overexpressing and control groups. qRT-PCR showed the probe effectively enriched circHECTD2 in the overexpressing group; consistently, IGF2BP3 was also significantly enriched in the circHECTD2 pulldown fraction (Fig. 3H), indicating potential interaction. RIP assays in Flag-IGF2BP3-overexpressing cells further confirmed that higher IGF2BP3 pulldown in the overexpressing group correlated with higher circHECTD2 levels vs. controls (Fig. 3I). These findings collectively demonstrate that IGF2BP3 interacts with circHECTD2 and regulates its stability. Co-localization was confirmed by immunofluorescence and FISH in FaDu and Tu686 cells (Fig. 3J; SCC9 results in Supplementary Fig. 6E) and tissue samples (Supplementary Fig. 6F).

### IGF2BP3 interacts with circHECTD2 through the KH3 domain

To define the precise binding interface between IGF2BP3 and circHECTD2, we first identified a consensus GGAC motif through analysis of MeRIP-seq data, which was highly consistent with findings reported by Huang et al. (Fig. 3K) [28]. Molecular docking simulations identified specific interactions between the KH3 domain of IGF2BP3 and the GGAC motif of circHECTD2 in the conformation with the lowest binding free energy. The analysis yielded an optimal binding score of -61.589 for the protein-nucleic acid complex, indicating a stable interaction mediated by multiple amino acid residues of IGF2BP3. The interaction profile primarily included hydrogen bonds, van der Waals forces, polar interactions, and hydrophobic interactions. Specifically, a total of 4 hydrogen bonds were detected, predominantly formed between lysine (LYS) and serine (SER) residues

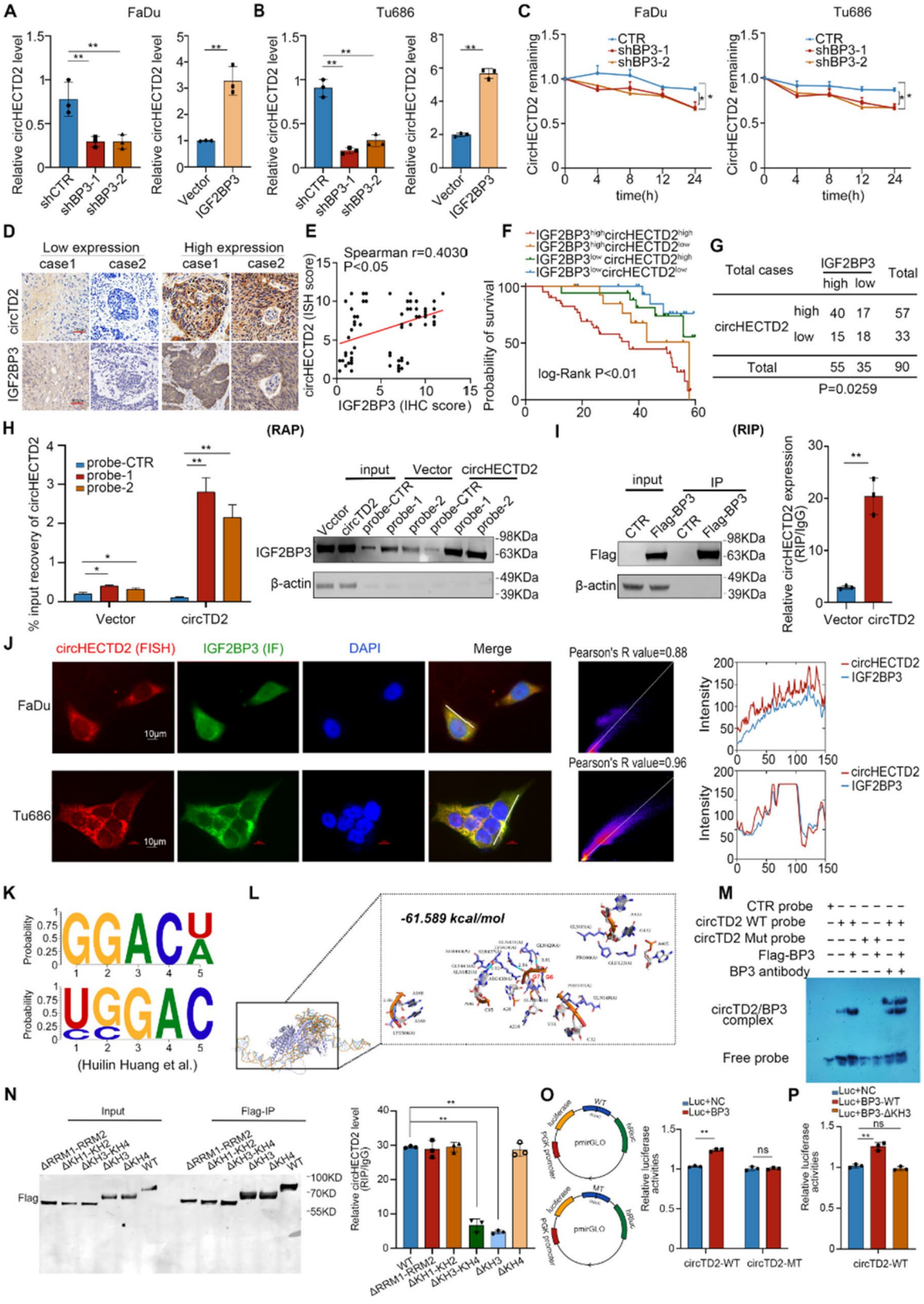


**Fig. 3** (See legend on next page.)

(See figure on previous page.)

**Fig. 3** IGF2BP3 Regulates circHECTD2 in HNSCC Through Interaction Mediated by the KH3 Domain. (**A-B**) qPCR analysis of circHECTD2 expression in IGF2BP3 knockdown, overexpression, and control groups in FaDu cells (**A**) and Tu686 cells (**B**). (**C**) qPCR analysis of the effect of actinomycin D treatment on circHECTD2 expression in shIGF2BP3-1/2 transfected FaDu and Tu686 cells relative to their respective controls. (**D**) ISH and IHC results of circHECTD2 and IGF2BP3 in tissue sections. (**E**) Spearman correlation analysis for ISH scores of circHECTD2 and IHC scores of IGF2BP3. (**F**) Survival curves of patients with high and low expression of IGF2BP3 and circHECTD2 revealed by HNSCC in IHC experiments, analyzed using the Kaplan-Meier method and log-rank test. (**G**) Association between expression levels of circHECTD2 and IGF2BP3 analyzed using chi-square test. (**H**) qPCR and western blot analysis to verify the RAP results of pLC5-circHECTD2 and the control group. (**I**) Western blot and qPCR to verify RIP results of Flag-IGF2BP3 and control groups. (**J**) Co-localization of IGF2BP3 and circHECTD2 was demonstrated by IF and FISH experiments in FaDu and Tu686 cells. (**K**) Consensus GGAC motif in the MeRIP-seq results. (**L**) Molecular docking pattern of IGF2BP3 protein and circHECTD2. Purple represents proteins, and brown represents nucleic acids. The right panel shows the interacting residues/bases. Dark blue indicates N atoms, red indicates O atoms, and light blue denotes the formed hydrogen bond interactions. Analysis showed that the optimal binding score between the protein and nucleic acid was −61.589, indicating an interaction between them involving multiple amino acids. The main types of interactions include hydrogen bonds, van der Waals interactions, polar interactions, and hydrophobic interactions. (**M**) RNA-EMSA assay showing the binding ability of purified IGF2BP3 with biotin-labeled oligonucleotides containing GGAC motif from circHECTD2. (**N**) Western blot and qPCR to verify RIP experiment results. (**O**) Mode pattern showing the dual-luciferase reporter vectors inserted with circHECTD2 WT or mutant sequences downstream of the pmirGLO promoter and the relative activities of luciferase detected after co-transfection of IGF2BP3 and negative control respectively. (**P**) Relative activities of luciferase detected after co-transfection of IGF2BP3 or IGF2BP3-ΔKH3 and negative control in pmirGLO-circHECTD2-WT. (**A-P**) BP3: IGF2BP3, circTD2: circHECTD2, CTR: negative control. Data are presented as mean ± SD, $*p < 0.05$, $**p < 0.01$, ns, not significant, using Student's t test

in the protein, and the phosphate groups (OP1, OP2) as well as ribose (O2') moieties in the nucleic acid; these hydrogen bonds are critical for stabilizing the protein-nucleic acid complex. Additionally, 30 non-bonded contacts were identified, mainly consisting of van der Waals interactions between various amino acid residues of the protein (e.g., LYS, SER, ALA, GLY, ARG, GLN, PHE, GLU, PRO) and the bases/ribose of the nucleic acid. Collectively, these hydrogen bonds and non-bonded contacts synergistically enhance the structural stability of the IGF2BP3-circHECTD2 complex (Fig. 3L). On the basis of these observations, we hypothesized that the GGAC motif serves as the binding region for binding of circHECTD2 to IGF2BP3, with the adenine residue within this motif being the methylation site. To test this hypothesis, we designed wild-type (WT) and mutant probes for circHECTD2 targeting this adenine residue (Supplementary Fig. 6G) and performed EMSA. Results showed that IGF2BP3 specifically bound to WT probes containing the GGAC motif, whereas no interaction was detected with mutant probes (Fig. 3M). As previously reported, IGF2BP3 contains six domains (Supplementary Fig. 6H) [28]. To identify the domain responsible for binding to circHECTD2, we constructed FLAG-tagged truncation mutants of IGF2BP3 and performed RIP assays. Results indicated that the KH3 domain is likely the key region mediating circHECTD2 binding (Fig. 3N). Subsequent luciferase reporter assays demonstrated that insertion of the WT circHECTD2 sequence into the 3'UTR of the reporter plasmid significantly enhanced relative luciferase activity via IGF2BP3 binding, whereas the mutant circHECTD2 sequence had no such effect (Fig. 3O). Furthermore, overexpression of the IGF2BP3-ΔKH3 mutant (lacking the KH3 domain) in pmirGLO-circHECTD2-GGAC-expressing cells abolished this increase in relative luciferase activity (Fig. 3P).

### IGF2BP3 stabilizes circHECTD2 through METTL3-mediated m$^6$A modification

To confirm that IGF2BP3 functions as the methylation-binding protein for the GGAC sequence, we performed pull-down assays using methylated single-stranded RNA bait containing the consensus sequence GG(m$^6$A)C and unmethylated control RNA. Results confirmed that IGF2BP3 selectively bound to the methylated bait with higher affinity than the unmethylated control (Fig. 4A). Next, we aimed to demonstrate that IGF2BP3 stabilizes circHECTD2 in a manner dependent on its methylated modification sites. We constructed two plasmids—H-circHECTD2-WT and H-circHECTD2-MT—each containing a nucleotide sequence of HA tag. The key difference was that H-circHECTD2-WT overexpressed the circHECTD2-GGAC sequence, while H-circHECTD2-MT overexpressed the circHECTD2-GGUC sequence (Fig. 4B). To verify the function of this methylation modification, we planned to conduct studies by enhancing or reducing its modification level. To this end, we first focused on the common "writers" and "erasers" of this methylation and successfully constructed small interfering RNAs (siRNAs) targeting nine related enzymes (Supplementary Fig. 7A). Subsequently, in cell models with individual knockdown of these nine enzymes, we detected the expression level of circHECTD2. The results (Supplementary Fig. 7B) showed that circHECTD2 levels were significantly decreased following knockdown of METTL3, RBM15, or RBM15B, while circHECTD2 was remarkably increased upon FTO or ALKBH5 knockdown. Notably, the reduction magnitude in the METTL3-knockdown group was more pronounced than that in the RBM15-, RBM15B-, FTO- or ALKBH5- knockdown

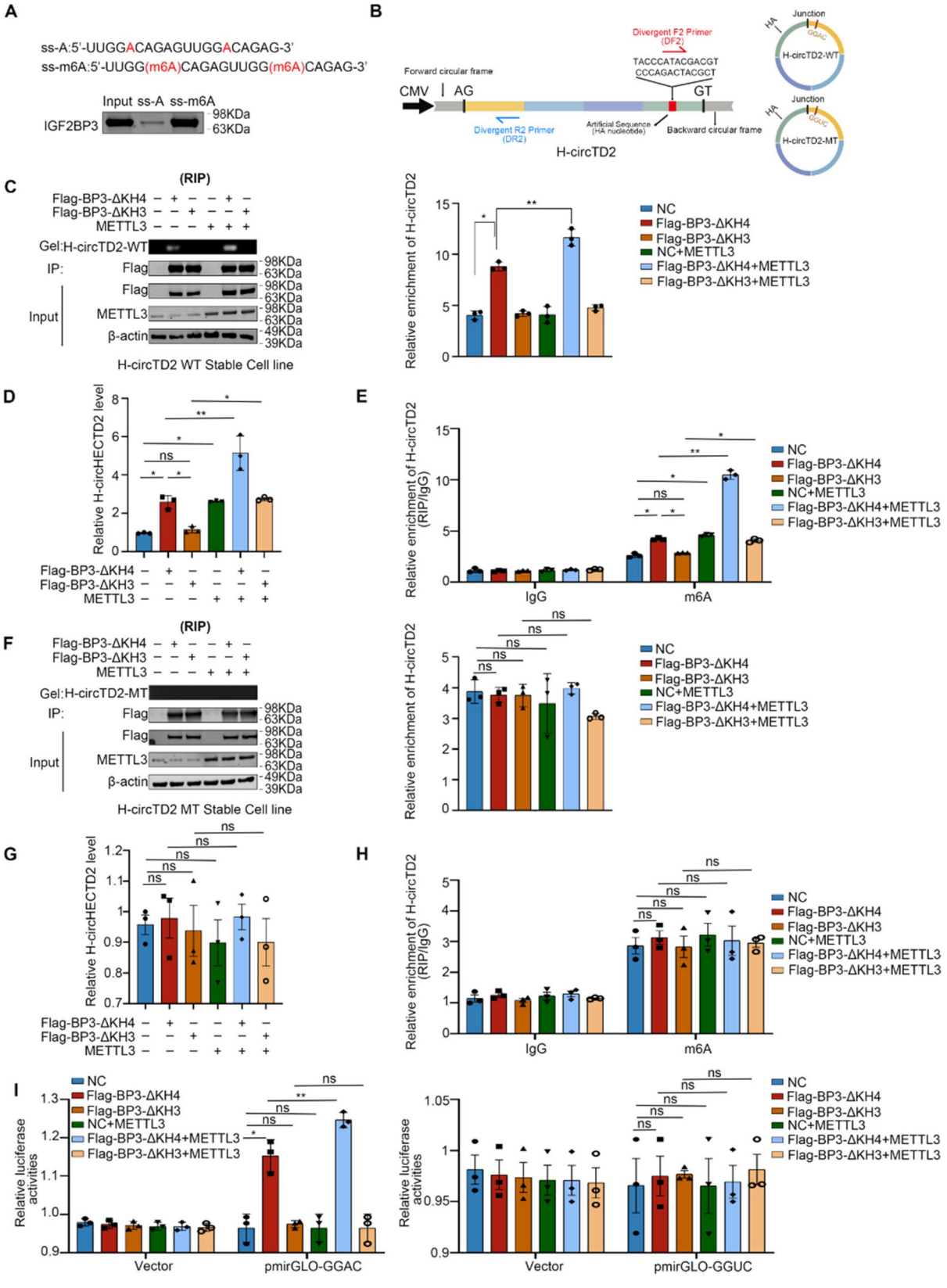


**Fig. 4** (See legend on next page.)

(See figure on previous page.)

**Fig. 4** IGF2BP3 stabilizes circHECTD2 through METTL3-mediated m$^6$A modification. (**A**) The binding ability of IGF2BP3 was identified by RAP using single-stranded RNA probes containing methylated or unmethylated adenosine. (**B**) Schematic diagrams of plasmid H-circHECTD2-WT and plasmid H-circHECTD2-MT. (**C**) Western blot and qPCR to verify RIP experiment results in H-circHECTD2-WT cells. (**D**) qPCR to verify the expression of circHECTD2 in H-circHECTD2-WT cells. (**E**) qPCR to verify the methylation level of circHECTD2 in H-circHECTD2-WT cells. (**F**) Western blot and qPCR to verify RIP experiment results in H-circHECTD2-MT cells. (**G**) qPCR to verify the expression of circHECTD2 in H-circHECTD2-MT cells. (**H**) qPCR to verify the methylation level of circHECTD2 in H-circHECTD2-MT cells. (**I**) Relative activities of luciferase after co-transfection of H-circHECTD2-WT in pmirGLO-circHECTD2-WT and pmirGLO-circHECTD2-MT. (**A-I**) BP3: IGF2BP3, circTD2: circHECTD2. Data are presented as mean ± SD, *$p < 0.05$, **$p < 0.01$, ns, not significant, using Student's t test

groups. In addition, we performed a correlation analysis between the qRT-PCR results, and the IHC and ISH results. The results indicated no correlation in the qRT-PCR results (Supplementary Fig. 7C–D), whereas a positive correlation between METTL3 and circHECTD2 was observed in the combined IHC and ISH results (Supplementary Fig. 7E). Furthermore, patients with high expression of both METTL3 and circHECTD2 exhibited poor prognosis (Supplementary Fig. 7F). To assess the impact of the IGF2BP3 KH3 domain on m$^6$A modification of circHECTD2, we performed RIP assays in six experimental groups using H-circHECTD2-WT stable cell lines. Overexpression of Flag-IGF2BP3-ΔKH4 or Flag-IGF2BP3-ΔKH3 allowed pull-down of IGF2BP3 via the Flag tag; however, only Flag-IGF2BP3-ΔKH4 successfully pulled down circHECTD2-WT; Flag-IGF2BP3-ΔKH3 did not. Moreover, co-overexpression of METTL3 resulted in increased circHECTD2 pull-down (Fig. 4C). qRT-PCR analysis of these six groups showed that overexpression of Flag-IGF2BP3-ΔKH4 increased circHECTD2 expression, with a more pronounced effect when Flag-IGF2BP3-ΔKH4 was co-overexpressed with METTL3. In contrast, overexpression of Flag-IGF2BP3-ΔKH3 had no such effect (Fig. 4D). MeRIP-qRT-PCR assays further revealed that overexpression of Flag-IGF2BP3-ΔKH4 elevated circHECTD2 methylation levels, whereas overexpression of Flag-IGF2BP3-ΔKH3 did not. Consistent with METTL3's role as an m$^6$A writer, METTL3 overexpression alone also increased circHECTD2 methylation levels (Fig. 4E). We repeated these experiments using H-circHECTD2-MT stable cell lines. RIP assays showed that overexpression of Flag-IGF2BP3-ΔKH4 pulled down only trace amounts of circHECTD2, with no enhancement upon co-overexpression of METTL3 (Fig. 4F). qRT-PCR analysis revealed no significant differences in circHECTD2 expression across the six groups (Fig. 4G), and MeRIP-qRT-PCR assays showed no detectable changes in circHECTD2 methylation levels (Fig. 4H). Luciferase reporter assays in these six groups yielded consistent results: stable transfection of pmirGLO-GGAC led to increased relative luciferase activity upon Flag-IGF2BP3-ΔKH4 overexpression, with further enhancement when METTL3 was co-overexpressed. In contrast, stable transfection of pmirGLO-GGUC resulted in no significant differences in relative luciferase activity between groups (Fig. 4I).

To address whether IGF2BP3 can regulate circHECTD2 after METTL3 perturbation, we further overexpressed IGF2BP3 in the context of METTL3 knockdown. The results showed that when METTL3 was reduced, IGF2BP3 overexpression still upregulated circHECTD2; however, the upregulatory effect was significantly attenuated due to the reduction in METTL3 (Supplementary Fig. 7G). To further clarify whether METTL3 is an essential component of this regulatory pathway, we attempted to directly target its substrate—the m$^6$A methylation sites on circHECTD2. For this purpose, we transfected cells with two exogenous circHECTD2 expression vectors, H-circTD2-WT and H-circTD2-WT with ablated m$^6$A methylation sites. The experimental results demonstrated that IGF2BP3 overexpression significantly upregulated the expression of wild-type circHECTD2, whereas it exerted no obvious regulatory effect on the expression of the MT circHECTD2 with deleted m$^6$A sites (Supplementary Fig. 7G), confirming that IGF2BP3's regulation of circHECTD2 is dependent on METTL3-mediated methylation.

Next, we sought to define how METTL3 knockdown affects the binding between IGF2BP3 and circHECTD2 by performing RIP assays. The results demonstrated that overexpression of Flag-IGF2BP3 efficiently enriched IGF2BP3 protein via the Flag tag, while successfully pulling down circHECTD2-WT; in contrast, concurrent METTL3 knockdown led to a significant reduction in the amount of precipitated circHECTD2 (Supplementary Fig. 8A). qRT-PCR analysis revealed that Flag-IGF2BP3 overexpression markedly upregulated the expression level of circHECTD2; whereas, when Flag-IGF2BP3 overexpression was combined with METTL3 knockdown, circHECTD2 expression was notably downregulated (Supplementary Fig. 8B). MeRIP-qRT-PCR assays further confirmed that Flag-IGF2BP3 overexpression enhanced the methylation level of circHECTD2, whereas concurrent METTL3 knockdown significantly inhibited the methylation of circHECTD2 (Supplementary Fig. 8C). Subsequent functional experiments also verified that METTL3 knockdown could effectively reverse the protumorigenic effect mediated by IGF2BP3 (Supplementary Figs. 8D–G).

To establish a link between this molecular mechanism and malignant phenotypes of HNSCC, we then performed functional assays in FaDu and Tu686 cells,

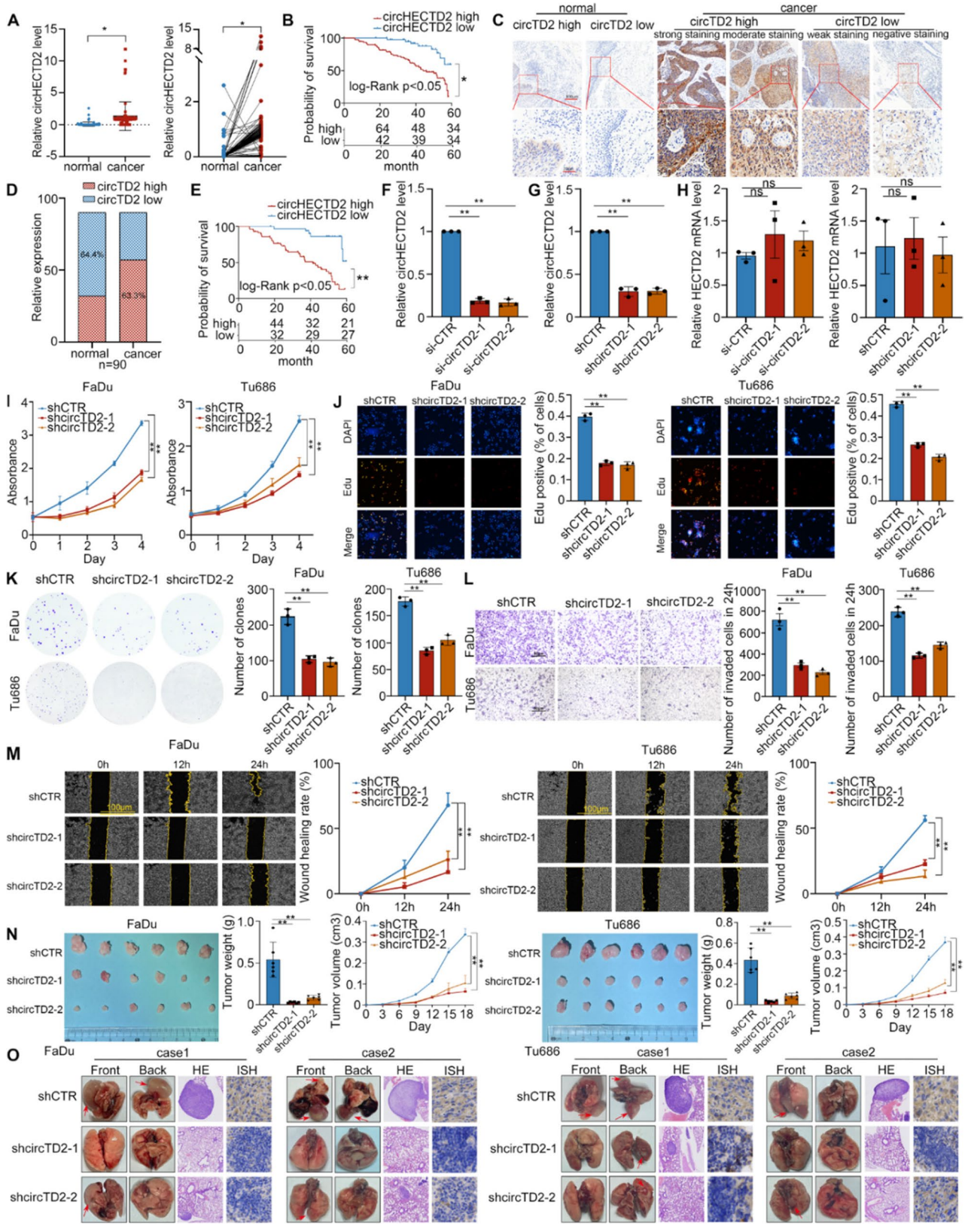


**Fig. 5** (See legend on next page.)

(See figure on previous page.)

**Fig. 5** circHECTD2 promotes progression of HNSCC in vivo and in vitro. (**A**) qPCR to verify the expression of circHECTD2 in HNSCC and adjacent non-tumor tissues ($n = 120$). Due to the non-normal distribution of the data, statistical analysis was performed using the Mann-Whitney U test. (**B**) Survival curves of patients with high and low expression of circHECTD2 revealed by HNSCC in qPCR experiments using Kaplan-Meier method and log-rank test. (**C**) The results of ISH in the tissues of 90 pairs of HNSCC and adjacent non-tumor tissues were divided into strong staining, moderate staining, weak staining, and negative staining. (**D**) The expression levels of HNSCC and adjacent non-tumor tissues in ISH results were analyzed. (**E**) Survival curves of patients with high and low circHECTD2 expression indicated by HNSCC in ISH experiment using Kaplan-Meier method and log-rank test. (**F**) qPCR to verify the circHECTD2 level in si-circHECTD2-1/2 and control groups. (**G**) The stable cell lines shcircHECTD2-1/2 were constructed by knockdown circHECTD2. (**H**) qPCR to verify the HECTD2 mRNA level in si-circHECTD2-1/2, sh-circHECTD2-1/2 and their control groups. (**I-M**) CCK-8 (**I**), EdU (**J**), colony formation (**K**), Transwell (**L**), and scratch wound healing assays (**M**) of sh-circHECTD2-1/2 and control groups in FaDu and Tu686 cells. (**N**) Cells of sh-circHECTD2-1/2 and control groups were injected subcutaneously into the armpit of nude mice ($n = 6$). Tumor volume was measured every three days, and growth curves were plotted. On the 19th day, the mice were killed, and tumors were excised and weighed. (**O**) Results of tumor dissection, hematoxylin-eosin (HE) staining, and IHC staining in nude mice with lung metastases established by tail vein injection of circHECTD2 knockdown and control FaDu and Tu686 cells. (**A-O**) Cancer: HNSCC tissues, normal: adjacent non-tumor tissues, BP3: IGF2BP3, circTD2: circHECTD2. Data are presented as mean ± SD, $^{*}p < 0.05$, $^{**}p < 0.01$, ns, not significant, using Student's t test

with groups including control, METTL3 overexpression, IGF2BP3 overexpression, METTL3 and IGF2BP3 co-overexpression, and parallel groups with circHECTD2-WT/MT transfection. Assays included CCK-8 assay (Supplementary Fig. 9A), EdU incorporation assay (Supplementary Fig. 9B), scratch wound healing assay (Supplementary Fig. 9C) and Transwell assay (Supplementary Fig. 9D). These results showed that in circHECTD2 WT, METTL3 and IGF2BP3 co-overexpression may more strongly enhance cell proliferation, migration, and invasion than each alone, while in the circHECTD2 MT, this promoting effect was largely abolished. Collectively, our data demonstrates that METTL3-mediated methylation may be a necessary prerequisite for IGF2BP3 to regulate circHECTD2, directly driving HNSCC malignant phenotypes.

### circHECTD2 promotes progression of HNSCC in vivo and in vitro

To clarify the role of circHECTD2 in HNSCC, we first detected circHECTD2 expression in 120 pairs of HNSCC and adjacent non-tumor tissues. Results showed that circHECTD2 expression was significantly higher in HNSCC tissues than in non-tumor tissues ($p < 0.05$) (Fig. 5A). Survival analysis based on qRT-PCR results indicated that patients with high circHECTD2 expression tended to have a poor prognosis (Fig. 5B). To further validate these findings, ISH was performed on the same 90 pairs of HNSCC and non-tumor tissues (Fig. 5C). Consistent with qRT-PCR results, ISH analysis confirmed significantly higher circHECTD2 expression in HNSCC tissues (Fig. 5D), and patients with high circHECTD2 levels had a worse prognosis (Fig. 5E). Analysis of correlations between circHECTD2 expression and clinicopathological features in the 120 cases revealed positive associations with tumor size, tumor differentiation, and American Joint Committee on Cancer clinical stage (Table 3). To explore the functional role of circHECTD2, we designed siRNAs targeting circHECTD2 (si-circHECTD2-1/2) (Fig. 5F) and established stable circHECTD2-knockdown cell lines (Fig. 5G). Notably, circHECTD2 knockdown did not affect the mRNA expression of its linear counterpart (Fig. 5H). A series of functional assays—including CCK-8 (Fig. 5I), EdU incorporation (Fig. 5J), colony formation (Fig. 5K), Transwell (Fig. 5L), and scratch wound healing assays (Fig. 5M)—were performed to evaluate changes in proliferation, migration, and invasion abilities in FaDu and Tu686 cells. Compared with the control, circHECTD2 knockdown significantly reduced these abilities, whereas circHECTD2 overexpression in SCC9 cells enhanced them (Supplementary Fig. 10). In vivo, FaDu and Tu686 cells with stable circHECTD2 knockdown were subcutaneously injected into nude mice to establish xenograft models. Tumor growth was significantly inhibited in the knockdown group, with a notable reduction in tumor weight compared with the control group (Fig. 5N). Additionally, tail vein injection of circHECTD2-knockdown FaDu and Tu686 cells were used to assess metastatic capacity. Subsequent hematoxylin-eosin and ISH staining of lung metastatic tumors showed that both metastatic potential and circHECTD2 expression were lower in the knockdown group than in the control group (Fig. 5O). Statistical data on metastatic lung nodules are provided in Supplementary Fig. 11. These results demonstrated that circHECTD2 overexpression enhances cell proliferation, invasion, and migration abilities, whereas its knockdown exerts the opposite effects, both in vitro and in vivo.

To verify that IGF2BP3 promotes HNSCC progression through circHECTD2, we performed rescue experiments in three groups: IGF2BP3-overexpressing cells, IGF2BP3-overexpressing cells with circHECTD2 knockdown, and control cells. Functional assays—including CCK-8 (Supplementary Fig. 12A), EdU incorporation (Supplementary Fig. 12B), Transwell (Supplementary Fig. 12C), and scratch wound healing assays (Supplementary Fig. 12D)—were conducted in three HNSCC cell lines: FaDu, Tu686, and SCC9. Results showed that circHECTD2 knockdown rescued the pro-tumorigenic effects of IGF2BP3 overexpression.

**Table 3** The relationship between circHECTD2 expression and the clinicopathological characteristics of 120 HNSCC patients

| Characteristics | Total 120 | circHECTD2 express | | $\chi^2$ | *P* Value |
|---|---|---|---|---|---|
| | | High | Low | | |
| Age (y) | | | | 0.9228 | 0.3367 |
| >=60 | 73 | 45 | 28 | | |
| <60 | 47 | 33 | 14 | | |
| Gender | | | | | |
| Male | 114 | 74 | 40 | 0.0077 | 0.9300 |
| Female | 6 | 4 | 2 | | |
| Drink | | | | 3.3800 | 0.0660 |
| No | 21 | 10 | 11 | | |
| Yes | 99 | 68 | 31 | | |
| T classification | | | | 9.8630 | 0.0198 |
| T1 | 27 | 16 | 11 | | |
| T2 | 50 | 27 | 23 | | |
| T3 | 34 | 26 | 8 | | |
| T4 | 9 | 9 | 0 | | |
| N classification | | | | 9.1160 | 0.0278 |
| N0 | 37 | 25 | 12 | | |
| N1 | 33 | 15 | 18 | | |
| N2 | 47 | 35 | 12 | | |
| N3 | 3 | 3 | 0 | | |
| Tumor differentiation | | | | 4.4180 | 0.1098 |
| Well | 24 | 13 | 11 | | |
| Moderate | 67 | 49 | 18 | | |
| Poor | 29 | 16 | 13 | | |
| AJCC stage | | | | 0.6092 | 0.8943 |
| I | 11 | 7 | 4 | | |
| II | 18 | 11 | 7 | | |
| III | 31 | 19 | 12 | | |
| IV | 60 | 41 | 19 | | |

#### CircHECTD2 absorbs hsa_miR_4310/7157-5p

It is well known that circRNA acts as a miRNA sponge [29] (Fig. 6A). Notably, numerous studies have demonstrated that a subset of these miRNAs inherently exert tumor-suppressive effects in various cancers[30, 31]. To identify miRNAs sponged by circHECTD2, we performed a bioinformatics analysis using miRanda and RNAhybrid databases, yielding six candidate miRNAs at the intersection (Fig. 6B). RAP assays were then conducted to validate the interaction of these candidate miRNAs with circHECTD2, and results revealed significant enrichment of two miRNAs, hsa-miR-4310 and hsa-miR-7157-5p (Fig. 6C). RIP assays further confirmed that both circHECTD2 and these miRNAs were co-precipitated with anti–Argonaute 2 antibodies, indicating incorporation of the miRNAs into the RNA-induced silencing complex (Fig. 6D). To visualize their colocalization, we designed FISH probes targeting circHECTD2 and these miRNAs. Fluorescence microscopy revealed significant colocalization of circHECTD2 with hsa-miR-4310 and hsa-miR-7157-5p in the cytoplasm of FaDu and Tu686 cells (Fig. 6E), which was further validated in SCC9 cells (Supplementary Fig. 13). Next, we investigated the functional impact of these miRNAs on HNSCC progression. We found that hsa-miR-4310/7157-5p mimics significantly inhibited proliferation, migration, and invasion in FaDu cells, as demonstrated by CCK-8 (Fig. 6F), EdU incorporation (Fig. 6G), colony formation, Transwell (Fig. 6H), and scratch wound healing assays (Fig. 6I). Similar results were observed in Tu686 and SCC9 cells (Supplementary Fig. 14), confirming the tumor-suppressive roles of these miRNAs.

To establish a functional axis between circHECTD2 and these miRNAs, we performed rescue experiments in HNSCC cell lines (FaDu, Tu686, SCC9) with three conditions: circHECTD2 overexpression, co-overexpression of circHECTD2 and hsa-miR-4310/7157-5p, and control. Functional assays—including CCK-8 (Supplementary Fig. 15A), EdU incorporation (Supplementary Fig. 15B), scratch wound healing (Supplementary Fig. 15C), Transwell assays (Supplementary Fig. 15D), and subcutaneous tumorigenesis assay in nude mice (Supplementary Fig. 16)—demonstrated that miRNA overexpression significantly attenuated the pro-tumorigenic effects of circHECTD2, including enhanced proliferation and metastasis. Collectively, these results suggest that overexpression of hsa_miR_4310/hsa_miR_7157-5p could rescue the pro-tumorigenic effects of circHECTD2.

To clarify the functional dependency between circHECTD2, miRNAs, and IGF2BP3, we co-manipulated these molecules in HNSCC cells, followed by functional assays (CCK-8, EdU, wound healing, and Transwell assays). As shown in Supplementary Fig. 17: compared with the control group, overexpression of wild-type circHECTD2 significantly promoted the proliferation, migration, and invasion of HNSCC cells; however, this oncogenic effect was partially reversed upon co-transfection with the target hsa_miR_4310/hsa_miR_7157-5p. Notably, further co-overexpression of IGF2BP3 rescued the inhibitory phenotype induced by hsa_miR_4310/hsa_miR_7157-5p, restoring the malignant biological behaviors of HNSCC cells. In contrast, when the IGF2BP3-binding sites of circHECTD2 were mutated, overexpression of IGF2BP3 exerted no significant effects on the functional phenotypes. Collectively, these results confirm that IGF2BP3 exerts its oncogenic function in HNSCC by binding to and upregulating circHECTD2, which in turn sponges target miRNAs to abrogate their downstream tumor-suppressive effects. Importantly, the binding between circHECTD2 and IGF2BP3 is a core prerequisite for the functional output of this regulatory axis, which suggests the critical role of m$^6$A modification of circHECTD2 in this process.

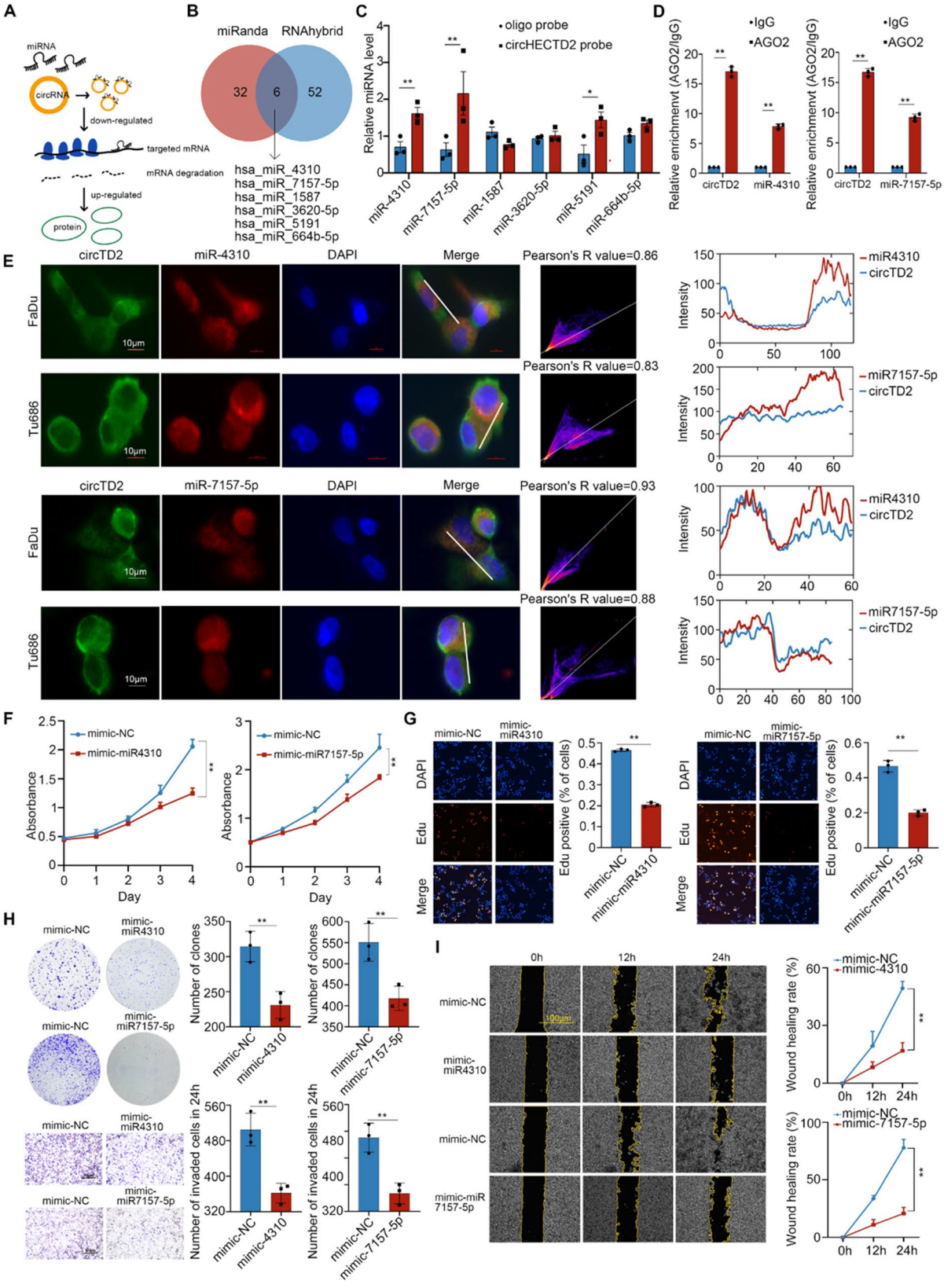


**Fig. 6** (See legend on next page.)

(See figure on previous page.)

**Fig. 6** CircHECTD2 absorbs hsa_miR_4310/7157-5p. (**A**) circRNA sponge model diagram. (**B**) The prediction about intersection of miRanda and RNAhybrid database of circHECTD2 absorbing miRNA. (**C**) The enrichment of six candidate miRNAs were evaluated by RAP assays using a circHECTD2 probe. (**D**) The interaction between circHECTD2 and miR-4310/miR-7157-5p was determined by RIP assays using anti-AGO2 or IgG antibodies. (**E**) Co-localization of circHECTD2 and miR-4310/ miR-7157-5p was demonstrated by FISH experiments in FaDu and Tu686 cells. (**F-I**) CCK-8 (**F**), EdU (**G**), colony formation, Transwell (**H**), and scratch wound healing assays (**I**) of mimic-miR-4310/7157-5p and control groups in FaDu cells. (**A-I**) circTD2: circHECTD2, miR-4310: hsa_miR_4310, miR-7157-5p: hsa_miR_7157-5p. Data are presented as mean ± SD, *$p < 0.05$, **$p < 0.01$, ns, not significant, using Student's t test

### IGF2BP3/circHECTD2 regulates SMAD2 by hsa_miR_4310/7157-5p

To delineate how the IGF2BP3/circHECTD2/hsa-miR-4310/hsa-miR-7157-5p axis regulates HNSCC progression, we performed RNA-seq on *IGF2BP3*-knockdown cell lines. Volcano plots highlighted differential expression of the *SMAD2* gene between the shIGF2BP3 and control groups (Fig. 7A). KEGG pathway enrichment analysis of sequencing data identified the top 10 enriched pathways (Fig. 7B), and subsequent Gene Set Enrichment Analysis prioritized the TGF-β signaling pathway for further investigation (Fig. 7C–D). qRT-PCR validation of the top 10 differentially expressed genes from RNA-seq confirmed consistent changes in mRNA levels upon IGF2BP3 knockdown or overexpression (Supplementary Fig. 18). Notably, TGF-β signaling-related genes (*SMAD2*, *BMP6*, *ACVR2B*) and *MYC* showed robust responses. Additionally, RNA-seq of circHECTD2-knockdown cells identified six overlapping downregulated genes in both knockdown groups (Fig. 7E), with *SMAD2* emerging as the most significantly downregulated gene in volcano plots (Fig. 7F). On the basis of these results, together with the *IGF2BP3*-knockdown sequencing results, *SMAD2* was selected as a key target for further study. Potential binding sites between circHECTD2, hsa-miR-4310/hsa-miR-7157-5p, and *SMAD2* were predicted using TargetScanHuman, and then mutant dual-luciferase reporter plasmids were constructed (Fig. 7G). Dual-luciferase assays showed that transfection with hsa-miR-4310/hsa-miR-7157-5p mimics significantly decreased luciferase activity in the pmirGLO-circHECTD2-WT and pmirGLO-SMAD2-WT groups, but not in the mutant groups (Fig. 7H). However, co-transfection with circHECTD2 restored the luciferase activity reduced by hsa-miR-4310/hsa-miR-7157-5p mimics in the pmirGLO-SMAD2-WT group (Fig. 7H). These results demonstrated that circHECTD2 upregulates *SMAD2* expression by sponging hsa-miR-4310 and hsa-miR-7157-5p. To confirm clinical relevance, we analyzed hsa-miR-4310/hsa-miR-7157-5p and *SMAD2* levels in 87 pairs of HNSCC and adjacent non-tumor tissues. hsa-miR-4310 and hsa-miR-7157-5p were downregulated and *SMAD2* was upregulated in tumor tissues (Fig. 7I). Spearman correlation analysis revealed negative correlations between hsa-miR-4310/hsa-miR-7157-5p and SMAD2 (Fig. 7J). We also analyzed the correlation between SMAD2 and circHECTD2 based on qRT-PCR results (Supplementary Fig. 19A), and the findings indicated a positive correlation between them. Survival analysis revealed that patients with low hsa-miR-4310/hsa-miR-7157-5p expression had worse overall survival (Fig. 7K), and patients with high *SMAD2* expression had worse overall survival (Supplementary Fig. 19B). To further analyze the impact of upstream and downstream genes in this regulatory axis on patients' survival prognosis, we performed survival prognostic analysis based on different expression combinations of IGF2BP3 with SMAD2, hsa-miR-4310, and hsa-miR-7157-5p. The results showed that patients with concurrent high expression of IGF2BP3 and SMAD2 had the poorest prognosis (Supplementary Fig. 19C); meanwhile, patients with high IGF2BP3 expression and low expression of hsa-miR-4310/hsa-miR-7157-5p also exhibited the worst survival outcome (Supplementary Fig. 19D–E). Western blot analysis revealed decreased protein levels of SMAD2 and phosphorylated SMAD2 (p-SMAD2) in cells with IGF2BP3 knockdown, circHECTD2 knockdown, or hsa-miR-4310/hsa-miR-7157-5p overexpression. Overexpression of IGF2BP3 or circHECTD2 increased the protein levels of SMAD2 and p-SMAD2, an effect that was reversed by overexpression of hsa-miR-4310/hsa-miR-7157-5p (Fig. 7L–M). All these results indicate that IGF2BP3/circHECTD2 regulates SMAD2 by hsa_miR_4310/7157-5p.

To clarify the clinical co-expression profiles of IGF2BP3, circHECTD2, and SMAD2 in clinical specimens, we performed immunohistochemistry (IHC) for IGF2BP3 and SMAD2, as well as in situ hybridization (ISH) for circHECTD2, on serial sections of patient tissues, followed by standardized quantitative scoring of the staining signals. Representative serial sections (Supplementary Fig. 20A) visually showed that in cases with high expression, all three molecules exhibited strong positive signals with consistent spatial localization, while weak signals were observed in low-expression cases, directly reflecting their co-localization in clinical tissues. Spearman correlation analysis further validated the positive correlations between SMAD2 and IGF2BP3, as well as between SMAD2 and circHECTD2. Contingency table analysis confirmed significant associations between SMAD2 expression and the expression of IGF2BP3 and circHECTD,

and survival analysis demonstrated that patients with co-high expression of IGF2BP3, circHECTD2, and SMAD2 had significantly poorer overall survival (Supplementary Fig. 20B–C), collectively supporting the clinical relevance of the co-expression pattern of these three molecules in the studied cohort.

### SMAD2 acts as a downstream effector of circHECTD2 to drive malignant progression of HNSCC

To verify the role of SMAD2 in HNSCC, we established stable cell lines with *SMAD2* knockdown (shSMAD2-1/2) in FaDu and Tu686 cells and with SMAD2 overexpression in SCC9 cells for subsequent functional experiments. A series of functional assays, including CCK-8 (Fig. 8A), EdU incorporation (Fig. 8B), colony formation (Fig. 8C), Transwell (Fig. 8D), and scratch wound healing assays (Fig. 8E), demonstrated that *SMAD2* knockdown significantly inhibited the proliferation, migration, and invasion abilities of FaDu and Tu686 cells. Parallel experiments in SCC9 cells showed that *SMAD2* overexpression enhanced these malignant phenotypes (Supplementary Fig. 21). Numerous studies have reported that the SMAD2 signaling pathway can promote tumor metastasis [32–34]. To further validate its role in vivo, we established a tumor metastasis model by tail vein injection of *SMAD2*-knockdown FaDu and Tu686 cells. hematoxylin-eosin staining and IHC analysis of lung metastases revealed that both the metastatic capacity and SMAD2 expression level in the knockdown group were significantly lower than those in the control group (Fig. 8F). Statistical data on metastatic lung nodules are provided in Supplementary Fig. 22. These results indicated that SMAD2 overexpression enhanced cell proliferation, invasion, and migration abilities, whereas *SMAD2* knockdown exerted opposite effects, both in vitro and in vivo.

To clarify whether hsa-miR-4310/hsa-miR-7157-5p affects HNSCC progression by degrading SMAD2 mRNA, we designed two sets of rescue experiments. The first set included three groups: hsa-miR-4310/hsa-miR-7157-5p inhibition group, hsa-miR-4310/hsa-miR-7157-5p inhibition combined with SMAD2 knockdown group, and control group. Results from CCK-8 (Supplementary Fig. 23A), EdU incorporation (Supplementary Fig. 23B), scratch wound healing (Supplementary Fig. 23C), and Transwell assays (Supplementary Fig. 23D) in three HNSCC cell lines (FaDu, Tu686, and SCC9) showed that knockdown of SMAD2 could reverse the promoting effect of hsa-miR-4310/hsa-miR-7157-5p inhibition on tumor progression. The second set of rescue experiments also consisted of three groups: hsa-miR-4310/hsa-miR-7157-5p mimic group, hsa-miR-4310/hsa-miR-7157-5p mimic combined with SMAD2 overexpression group, and control group. Consistent with the first set of experiments, results from CCK-8 (Supplementary Fig. 24A), EdU incorporation (Supplementary Fig. 24B), scratch wound healing (Supplementary Fig. 24C), and Transwell assays (Supplementary Fig. 24D) in three HNSCC cell lines (FaDu and Tu686) showed that overexpression of SMAD2 could abrogate the inhibitory effect of hsa-miR-4310/hsa-miR-7157-5p mimic on tumor progression.

To clarify whether circHECTD2 affects the progression of head and neck squamous cell carcinoma (HNSCC) by degrading SMAD2 mRNA, we designed two rescue experiments. The first rescue experiment included three groups: the circHECTD2 overexpression group, the circHECTD2 overexpression combined with SMAD2 knockdown group, and the control group; the second rescue experiment also consisted of three groups: the circHECTD2 knockdown group, the circHECTD2 knockdown combined with SMAD2 overexpression group, and the control group. CCK-8 assay (Supplementary Fig. 25A), EdU incorporation assay (Supplementary Fig. 25B), scratch wound healing assay (Supplementary Fig. 25C), and Transwell assay (Supplementary Fig. 25D) were performed in FaDu and Tu686 cell lines. The results showed that knockdown of SMAD2 could reverse the pro-tumor progression effect induced by circHECTD2 overexpression, while overexpression of SMAD2 could reverse the tumor-suppressive effect caused by circHECTD2 knockdown.

## Discussion

As a stable form of RNA, circRNAs contribute to the initiation and progression of multiple tumors by inhibiting apoptosis [35] and promoting invasion, metastasis [36], and angiogenesis [37]. A multitude of studies have demonstrated that circRNAs regulate key cancer-related signaling pathways, including the Wnt/β-catenin pathway [38], AKT/mTOR autophagy pathway [39], and MAPK pathway [40]. $m^6A$ modification is one of the most common RNA methylation modifications. $m^6A$ modification is one of the most prevalent RNA methylation modifications. $m^6A$ modification is regulated by three classes of molecules: $m^6A$ methyltransferases ("writers"), such as METTL3/14 and WTAP [41, 42]; $m^6A$ demethylases ("erasers"), including FTO and ALKBH5 [43, 44]; and $m^6A$ recognition proteins ("readers"), such as YTHDF1/2/3 and IGF2BPs [45, 46]. Accumulating evidence indicates that $m^6A$ modification of circRNAs participates in the initiation and development of various cancers, including breast cancer [47], lung cancer [48], liver cancer [49], melanoma [50] and other cancers, by regulating circRNA stability, translation, and interactions with proteins. However, the biological roles and underlying mechanisms of $m^6A$-modified circRNAs in HNSCC remain poorly understood.

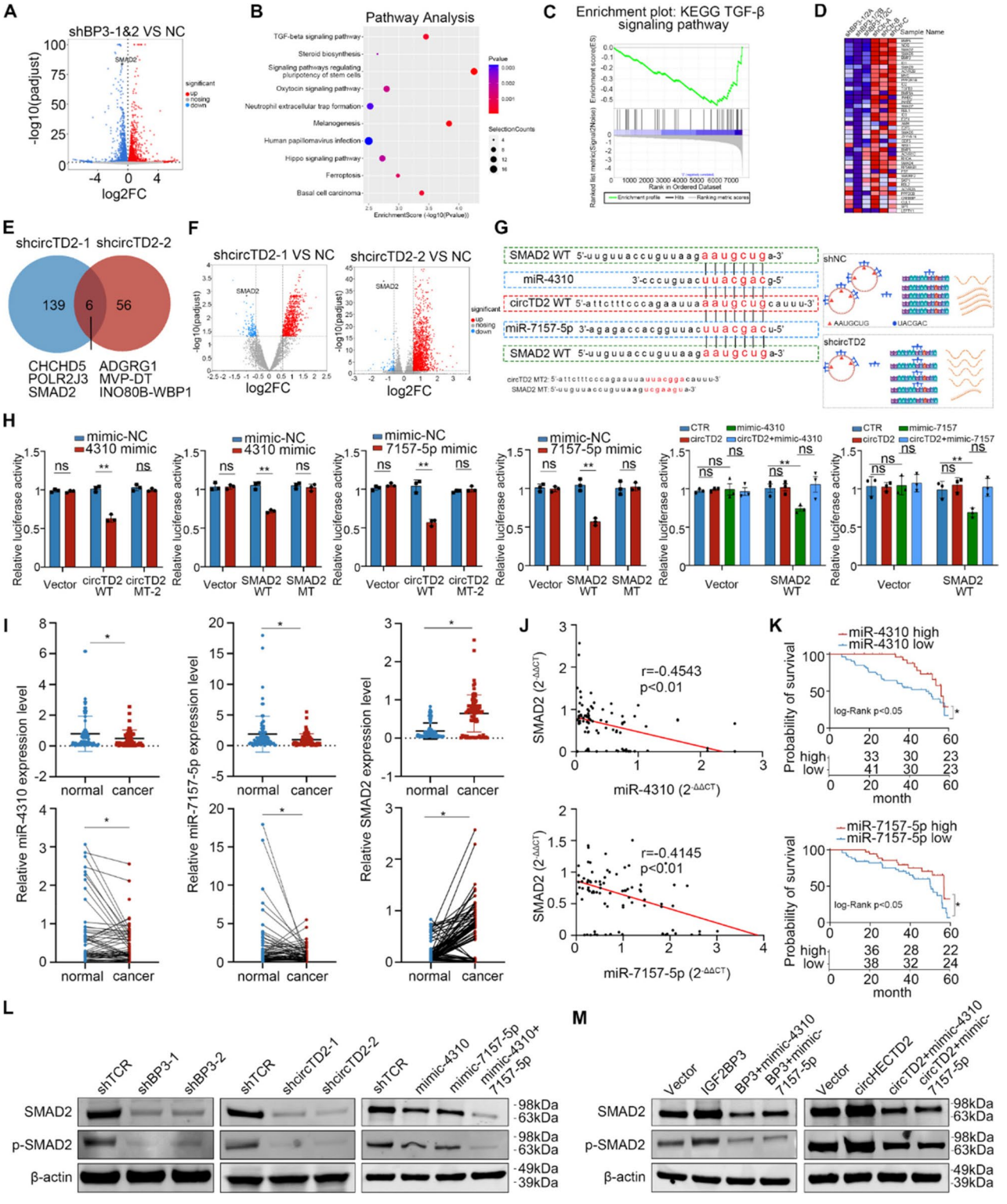


**Fig. 7** (See legend on next page.)

To further explore the molecular mechanisms underlying differential m$^6$A modification of circRNAs in HNSCC, we conducted qRT-PCR assays to detect the expression of common m$^6$A modification-related writers, readers, and erasers, and we found that IGF2BP3 was significantly upregulated in HNSCC. Recent studies have identified IGF2BP3 as a novel oncogenic factor in various solid tumors, including melanoma [51], kidney

(See figure on previous page.)

**Fig. 7** IGF2BP3/circHECTD2 regulates SMAD2 by hsa_miR_4310/7157-5p. (**A**) Volcano plot of RNA-seq on the IGF2BP3 knockdown cell lines. (**B**) KEGG enrichment analysis of two IGF2BP3 knockdown cell lines. (**C**) Gene set enrichment analysis of the TGF-β signaling pathway. (**D**) Heat map of genes associated with the TGF-β pathway between shIGF2BP3-1/2 and control groups. (**E**) Venn diagram of RNA-seq on the two circHECTD2 knockdown cell lines. (**F**) Volcano plot of RNA-seq on the two circHECTD2 knockdown cell lines. (**G**) CircHECTD2, hsa_miR_4310/hsa_miR_7157-5p, and SMAD2 binding sites in TargetScanHuman and constructed mutated dual-luciferase reporter plasmids. (**H**) The relative activities of luciferase were detected after co-transfection of miR-4310/miR-7157-5p mimic circHECTD2 and mimic-NC. (**I**) qPCR result of hsa_miR_4310, hsa_miR_7157-5p, and SMAD2 expression in HNSCC and adjacent non-tumor tissues ($n=87$). Due to the non-normal distribution of the data, statistical analysis was performed using the Mann-Whitney U test. (**J**) Spearman correlation analysis of qPCR results of hsa_miR_4310/ hsa_miR_7157-5p and SMAD2 expression levels. (**K**) Survival curves of patients with high and low miR-4310/7157-5p expression indicated by HNSCC in qPCR experiment using Kaplan-Meier method and log-rank test. (**L**) Western blot was performed to detect SMAD2 and p-SMAD2 protein expression levels in cells with *IGF2BP3* knockdown, circHECTD2 knockdown, or hsa_miR_4310/hsa_miR_7157-5p overexpression. (**M**) Western blot was performed to detect SMAD2 and p-SMAD2 protein expression levels in cells with *IGF2BP3* overexpression, circHECTD2 overexpression, or hsa_miR_4310/hsa_miR_7157-5p overexpression. (**A-M**) BP3: IGF2BP3, cancer: HNSCC tissues, circTD2: circHECTD2, miR-4310/4310: hsa_miR_4310, miR-7157-5p/7157-5p: hsa_miR_7157-5p, MT: mutant, normal: adjacent non-tumor tissues. Data are presented as mean ± SD, $*p<0.05$, $**p<0.01$, ns, not significant, using Student's t test

cancer [52], thyroid cancer [53], and liver cancer [54], with high IGF2BP3 expression correlating with metastasis and poor prognosis. However, the oncogenic role of IGF2BP3 in HNSCC remains unclear. Herein, we demonstrated that high IGF2BP3 expression is associated with poor prognosis in hypopharyngeal cancer. Loss-of-function experiments showed that IGF2BP3 promotes cancer cell proliferation, migration, and invasion, indicating its oncogenic role in HNSCC. These findings suggest that IGF2BP3 could serve as a therapeutic target and a potential biomarker for clinical diagnosis and prognostic evaluation of HNSCC.

Through circRNA-seq and MeRIP-seq analyses following IGF2BP3 downregulation, we identified circHECTD2 as a potential downstream target of IGF2BP3. We validated circHECTD2's circular structure and subcellular localization and confirmed that it also promotes HNSCC proliferation and migration. We investigated whether IGF2BP3 regulates the expression of HECTD2 mRNA. Our preliminary qRT-PCR results showed that IGF2BP3 has no regulatory effect on HECTD2 mRNA expression. The key distinction between linear HECTD2 mRNA and circHECTD2 lies in the junction site generated by the back-splicing event of the circular RNA—a feature that is absent in the linear transcript. Our sequence analysis confirmed that the GGAC motif is located 6 base pairs downstream of the junction site of circHECTD2. We speculated that circHECTD2 adopts a closed circular topology due to back-splicing, whereas linear HECTD2 mRNA exists in a linear conformation. Such differences in topological conformations may lead to distinct secondary and tertiary structures, which in turn could contribute to the potential differential binding affinity between these two RNA isoforms and IGF2BP3. Our study demonstrated not only the interaction between the KH3 domain of IGF2BP3 and the GGAC motif of circHECTD2 but also the regulatory effect of IGF2BP3 on the expression level and methylation status of circHECTD2 in both tissues and cells. IGF2BP3 contains six canonical RNA-binding domains: two N-terminal RNA recognition motifs and four C-terminal hnRNP-K homology (KH) domains [55]. In vitro studies have shown that stabilization of the IGF2BP3-RNA complex is primarily mediated by the KH3 domain, which may contribute to the binding of IGF2BP3 to the MYC coding region stability determinant (MYC-CRD) [28]. In the work reported here, we found that the KH3 domain of IGF2BP3 is also essential for its interaction with circHECTD2 and for circHECTD2 methylation.

IGF2BP3 stabilizes the expression of circHECTD2 by binding to its methylated form, while METTL3-mediated methylation of circHECTD2 not only enhances the interaction between IGF2BP3 and circHECTD2 but also improves the stability of circHECTD2. Based on our own experimental data and existing research evidence, we have identified METTL3 as the key methyltransferase mediating the methylation of circHECTD2. Specifically, after performing knockdown screening on 9 common $m^6A$ "writers" and "erasers", We found that knockdown of METTL3, RBM15, or RBM15B all significantly reduced the expression level of circHECTD2, while circHECTD2 was significantly increased upon FTO or ALKBH5 knockdown. Among these groups, the downregulation of circHECTD2 in the METTL3-knockdown group was the most pronounced. Mechanistically, as the core catalytic subunit of the $m^6A$ methyltransferase complex, METTL3 has inherent methyltransferase activity [56]; in contrast, RBM15 and RBM15B mainly function as auxiliary recruitment factors, lacking independent catalytic capacity and only being able to assist the methyltransferase complex in localizing to target RNAs [57]. Given that the core of this study is to decipher the regulatory mechanism of methylation modification on the stability of circHECTD2, selecting METTL3, which has dominant function and catalytic necessity, is crucial for effectively regulating the methylation level of circHECTD2 and verifying its biological significance. The specific molecular mechanism underlying the high expression of IGF2BP3 in HNSCC still needs further investigation.

circRNAs exert a miRNA sponging effect. Through online prediction and experimental validation, we identified two miRNAs (hsa-miR-4310 and hsa-miR-7157-5p)

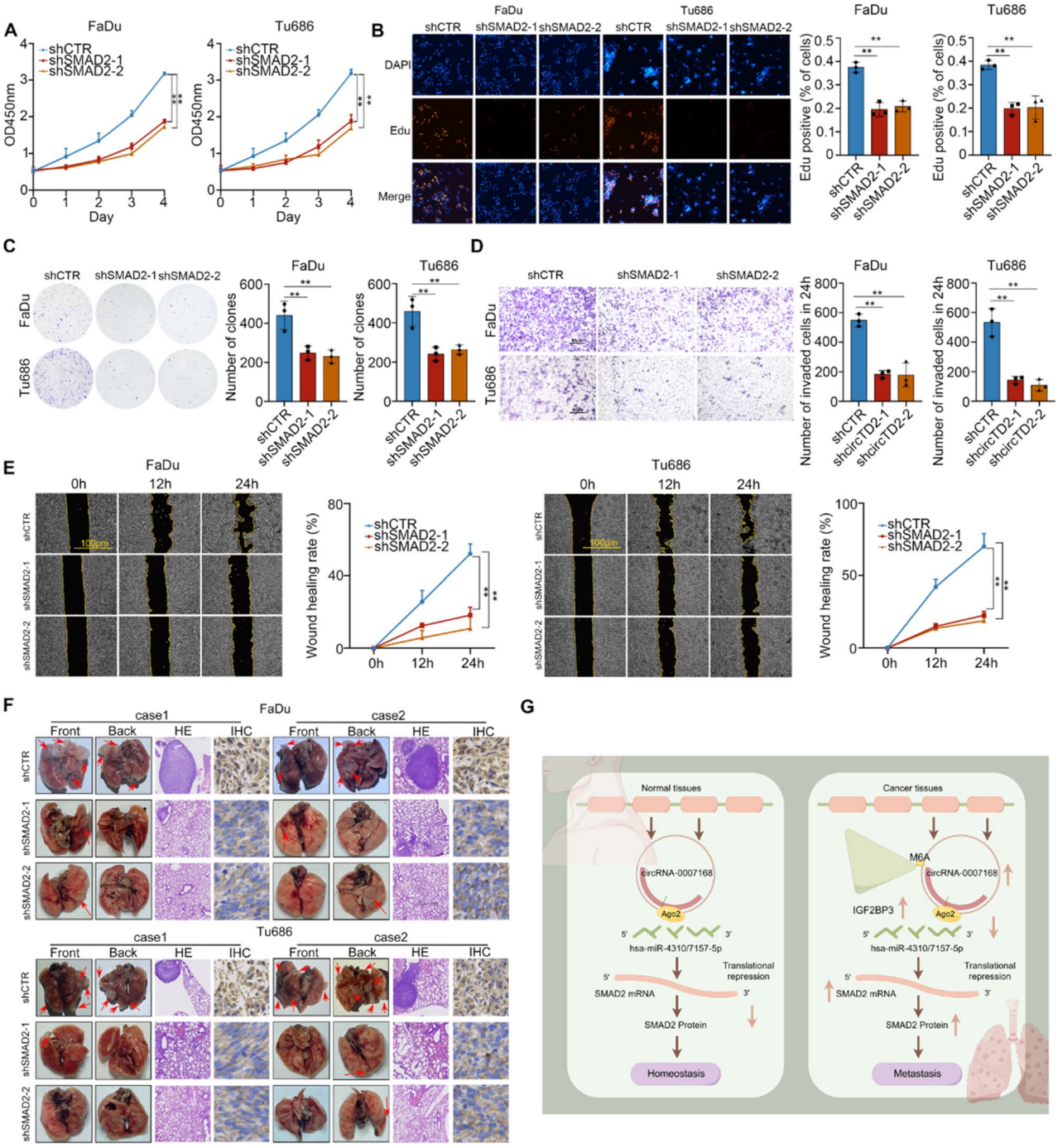


**Fig. 8** SMAD2 affects the proliferation, invasion, and metastasis of HNSCC. (**A-E**) CCK-8 (**A**), EdU (**B**), colony formation (**C**), Transwell (**D**), and scratch wound healing assays (**E**) of SMAD2 knockdown and control groups in FaDu and Tu686 cells. (**F**) Metastatic tumors and their hematoxylin-eosin and IHC staining in SMAD2 knockdown and control groups. (**G**) Mechanism diagram of IGF2BP3 promoting progression of HNSCC by stabilizing circHECTD2 in a $m^6A$ modification-dependent manner. Data are presented as mean ± SD, $^*p < 0.05$, $^{**}p < 0.01$, ns, not significant, using Student's t test

that are potentially adsorbed by circHECTD2. We verified the interaction between circHECTD2 and hsa-miR-4310/hsa-miR-7157-5p and found that adsorption of hsa-miR-4310/hsa-miR-7157-5p by circHECTD2 reduces the degradation of *SMAD2* mRNA, thereby promoting the proliferation, invasion, migration, and metastasis of HNSCC cells. Meanwhile, KEGG and gene set enrichment analyses of RNA-seq data suggested that the IGF2BP3/circHECTD2/hsa-miR-4310/hsa-miR-7157-5p/SMAD2 signaling pathway may represent a critical pathway involved in regulating HNSCC progression.

Furthermore, our experiments confirmed that knockdown or overexpression of *IGF2BP3*, circHECTD2, or hsa-miR-4310/hsa-miR-7157-5p led to corresponding changes in the expression levels of *SMAD2* in this signaling pathway. Notably, in the IGF2BP3/circHECTD2/hsa-miR-4310/hsa-miR-7157-5p axis, knockdown or overexpression of downstream molecules could affect the tumor-related effects of upstream molecules. These findings expand our understanding of the regulatory mechanism underlying IGF2BP3 function in tumor cells, which is mediated by the direct binding of circRNA to IGF2BP3. In summary, these results indicate that targeting m$^6$A modification-related readers and circular RNAs may serve as a potential therapeutic strategy for cancer treatment in the future.

Despite the meaningful findings presented above, this study has several inherent limitations that warrant explicit acknowledgment. First, the lack of in vivo therapeutic intervention experiments constitutes a major constraint—we have not validated the therapeutic potential of targeting the IGF2BP3/circHECTD2 axis via small-molecule inhibitors, antisense oligonucleotides, or siRNAs in animal models. While in vitro data confirm the oncogenic role of this axis, its translational value in clinical settings remains to be further verified through rigorous preclinical studies. Second, the potential off-target effects of targeting strategies have not been fully explored: inhibiting IGF2BP3 may disrupt the stability of other critical RNA targets beyond circHECTD2, and oligonucleotide-based strategies targeting circHECTD2 (e.g., siRNAs) might inadvertently affect its host gene HECTD2 or other RNAs with similar sequences. In future research, we will focus on developing specific targeting agents and conducting in vivo efficacy and safety evaluations to advance the translational application potential of this regulatory axis.

## Conclusion

In conclusion, our research suggested that IGF2BP3 and circHECTD2 were important tumor promoters of HNSCC. Functionally, IGF2BP3 and circHECTD2 could promote the proliferation, migration, and invasion of HNSCC cell lines. In the mechanism, circHECTD2 interacted with IGF2BP3, while IGF2BP3 and METTL3 modified m$^6$A together to stabilize the structure of circHECTD2. CircHECTD2 acted as a molecular sponge to adsorb hsa_miR_4310/hsa_miR_7157-5p, which promoted the expression of SMAD2. Our study identified circHECTD2 as a potential endogenous marker, broadening the therapeutic management options for HNSCC.

### Abbreviations

| | |
|---|---|
| CCK-8 | Cell Counting Kit-8 |
| circRNAs | Circular RNAs |
| DMEM | Dulbecco's modified Eagle medium |
| EdU | 5-ethynyl-2′-deoxyuridine |
| EMSA | Electrophoretic mobility shift assay |
| FISH | Fluorescence in situ hybridization |
| HNSCC | Head and neck squamous cell carcinoma |
| IHC | Immunohistochemistry |
| RNA-ISH | RNA in situ hybridization |
| KH | hnRNP-K homology |
| LSCC | Laryngeal squamous cell carcinoma |
| LYPD3 | LY6/PLAUR domain-containing 3 |
| m$^6$A | N6-methyladenosine |
| MeRIP | m$^6$A methylated RNA immunoprecipitation |
| MeRIP-seq | Methylated RNA immunoprecipitation sequencing |
| METTL3 | 3′-untranslated regions |
| miRNAs | MicroRNAs |
| qRT-PCR | Reverse transcription–quantitative polymerase chain reaction |
| RAP | RNA antisense purification |
| RIP | RNA immunoprecipitation |
| RLU | Relative light unit |
| siRNAs | Small interfering RNAs |
| WT | Wild-type |

## Supplementary Information

The online version contains supplementary material available at https://doi.org/10.1186/s12943-026-02619-4.

Supplementary Material 1.

### Authors' contributions

DL and FC conceived and designed the experiments; KW performed the experiments and wrote the manuscript; TP conducted bioinformatics analysis and statistics. XS and YZ assisted animal model construction; SW, YW, ZL, CD, JL, DS, WL, DW, SC, JL, JF GL and NG provided critical comments and suggestions; LC and JZ collected the tissue specimens; DL and FC revised the manuscript. All authors read and approved the final manuscript.

### Funding

This work was supported by the National Natural Science Foundation of China (No. 82471149), Key Technology Research and Development Program of Shandong Province (2025CXGC010603) and the Natural Science Foundation of Shandong Province (ZR2021QC062 and ZR2023MH153).

### Data availability

The whole-genome methylation sequencing and transcriptome sequencing datagenerated and analyzed during the current study have been deposited in the Gene Expression Omnibus (GEO) database under the accession number GSE313611.All other relevant data supporting the findings of this study are available from the corresponding author upon reasonable request.

## Declarations

### Ethics approval and consent to participate

The use of HNSCC tissues and matched adjacent non-tumor tissues in this study were approved by the Ethics Committee of Qilu Hospital of Shandong University (KYLL-2020(KS)-320). All animal care and experimental procedures were conducted in accordance with the guidelines of the Animal Care and Use Committee and approved by Qilu Hospital of Shandong University (KYLL-2023(ZM)-150).

### Competing interests

The authors declare no competing interests.

### Author details

[1]Department of Otorhinolaryngology, Qilu Hospital of Shandong University, Jinan, Shandong, China
[2]NHC Key Laboratory of Otorhinolaryngology (Shandong University), Jinan, Shandong, China
[3]Team of Digital Intelligence Health Management & Decision, (Shandong University), Jinan, Shandong, China

[4]Department of Otolaryngology, Head and Neck Surgery, West China Hospital, Sichuan University, Chengdu, China
[5]Head and Neck Surgical Center, West China Hospital, Sichuan University, Chengdu, China
[6]Department of Head and Neck Surgery, Beijing Tongren Hospital, Capital Medical University, Dongjiaomin lane No. 1, Dongcheng District, Beijing 100101, China
[7]Department of Head and Neck Surgery, The University of Texas MD Anderson Cancer Center, Houston, TX 77030, USA

Received: 9 October 2025 / Accepted: 13 February 2026
Published online: 02 March 2026

**References**

1. Johnson DE, Burtness B, Leemans CR, Lui VWY, Bauman JE, Grandis JR. Head and neck squamous cell carcinoma. Nat Rev Dis Primers. 2020;6(1):92.
2. Garneau JC, Bakst RL, Miles BA. Hypopharyngeal cancer: A state of the art review. Oral Oncol. 2018;86:244–50.
3. Ferlay J, Colombet M, Soerjomataram I, Mathers C, Parkin DM, Pineros M, et al. Estimating the global cancer incidence and mortality in 2018: GLOBOCAN sources and methods. Int J Cancer. 2019;144(8):1941–53.
4. Soerjomataram I, Bray F. Planning for tomorrow: global cancer incidence and the role of prevention 2020–2070. Nat Rev Clin Oncol. 2021;18(10):663–72.
5. Kristensen LS, Andersen MS, Stagsted LVW, Ebbesen KK, Hansen TB, Kjems J. The biogenesis, biology and characterization of circular RNAs. Nat Rev Genet. 2019;20(11):675–91.
6. Li Y, Zheng Q, Bao C, Li S, Guo W, Zhao J, et al. Circular RNA is enriched and stable in exosomes: a promising biomarker for cancer diagnosis. Cell Res. 2015;25(8):981–4.
7. Zhang Y, Yao R, Li M, Fang C, Feng K, Chen X, et al. CircTTC13 promotes sorafenib resistance in hepatocellular carcinoma through the inhibition of ferroptosis by targeting the miR-513a-5p/SLC7A11 axis. Mol Cancer. 2025;24(1):32.
8. Patop IL, Wust S, Kadener S. Past, present, and future of circRNAs. EMBO J. 2019;38(16):e100836.
9. Ge L, Sun Y, Shi Y, Liu G, Teng F, Geng Z, et al. Plasma circRNA microarray profiling identifies novel circRNA biomarkers for the diagnosis of ovarian cancer. J Ovarian Res. 2022;15(1):58.
10. Luo YH, Yang YP, Chien CS, Yarmishyn AA, Ishola AA, Chien Y et al. Plasma level of circular RNA hsa_circ_0000190 correlates with tumor progression and poor treatment response in advanced lung cancers. Cancers (Basel). 2020;12(7):1740.
11. Roy S, Kanda M, Nomura S, Zhu Z, Toiyama Y, Taketomi A, et al. Diagnostic efficacy of circular RNAs as noninvasive, liquid biopsy biomarkers for early detection of gastric cancer. Mol Cancer. 2022;21(1):42.
12. Wang Y, Chang F, Li Z, Duan C, Sun X, Wang S et al. CircTP53/USP10/p53 signaling Axis as a novel regulator of progression and prognosis of head and neck squamous cell carcinoma. Adv Sci (Weinh). 2025;12(30):e14961.
13. Jiang S, Ou L, Wang Y, Su K, Chen Z, He L, et al. CircPRMT5, a Potential Salivary Biomarker, Facilitates the Progression of Head and Neck Squamous Cell Carcinoma via the IGF2BP3-SERPINE1 Pathway. Int J Nanomed. 2025;20:1597–613.
14. Ge J, Meng Y, Guo J, Chen P, Wang J, Shi L, et al. Human papillomavirus-encoded circular RNA circE7 promotes immune evasion in head and neck squamous cell carcinoma. Nat Commun. 2024;15(1):8609.
15. Wang T, Kong S, Tao M, Ju S. The potential role of RNA N6-methyladenosine in Cancer progression. Mol Cancer. 2020;19(1):88.
16. Zaccara S, Ries RJ, Jaffrey SR. Reading, writing and erasing mRNA methylation. Nat Rev Mol Cell Biol. 2019;20(10):608–24.
17. Knuckles P, Buhler M. Adenosine methylation as a molecular imprint defining the fate of RNA. FEBS Lett. 2018;592(17):2845–59.
18. Jones AN, Tikhaia E, Mourao A, Sattler M. Structural effects of m6A modification of the Xist A-repeat AUCG tetraloop and its recognition by YTHDC1. Nucleic Acids Res. 2022;50(4):2350–62.
19. Kierzek E, Zhang X, Watson RM, Kennedy SD, Szabat M, Kierzek R, et al. Secondary structure prediction for RNA sequences including N(6)-methyladenosine. Nat Commun. 2022;13(1):1271.
20. Szabat M, Prochota M, Kierzek R, Kierzek E, Mathews DH. A Test and Refinement of Folding Free Energy Nearest Neighbor Parameters for RNA Including N(6)-Methyladenosine. J Mol Biol. 2022;434(18):167632.
21. Jiang X, Liu B, Nie Z, Duan L, Xiong Q, Jin Z, et al. The role of m6A modification in the biological functions and diseases. Signal Transduct Target Ther. 2021;6(1):74.
22. Liu ZX, Li LM, Sun HL, Liu SM. Link Between m6A Modification and Cancers. Front Bioeng Biotechnol. 2018;6:89.
23. Niu X, Yang Y, Ren Y, Zhou S, Mao Q, Wang Y. Crosstalk between m(6)A regulators and mRNA during cancer progression. Oncogene. 2022;41(39):4407–19.
24. Huang F, Ren Y, Hua Y, Wang Y, Li R, Ji N, et al. m6A-dependent mature miR-151-5p accelerates the malignant process of HNSCC by targeting LYPD3. Mol Biomed. 2024;5(1):27.
25. Zhao K, Chen L, Xie Y, Ren N, Li J, Zhai X, et al. m6A/HOXA10-AS/ITGA6 axis aggravates oxidative resistance and malignant progression of laryngeal squamous cell carcinoma through regulating Notch and Keap1/Nrf2 pathways. Cancer Lett. 2024;587:216735.
26. Yang L, Yan B, Qu L, Ren J, Li Q, Wang J, et al. IGF2BP3 Regulates TMA7-mediated Autophagy and Cisplatin Resistance in Laryngeal Cancer via m6A RNA Methylation. Int J Biol Sci. 2023;19(5):1382–400.
27. Li C, Guan R, Li W, Wei D, Cao S, Xu C, et al. Single-cell RNA sequencing reveals tumor immune microenvironment in human hypopharyngeal squamous cell carcinoma and lymphatic metastasis. Front Immunol. 2023;14:1168191.
28. Huang H, Weng H, Sun W, Qin X, Shi H, Wu H, et al. Recognition of RNA N(6)-methyladenosine by IGF2BP proteins enhances mRNA stability and translation. Nat Cell Biol. 2018;20(3):285–95.
29. Zhang W, Xu C, Yang Z, Zhou J, Peng W, Zhang X, et al. Circular RNAs in tumor immunity and immunotherapy. Mol Cancer. 2024;23(1):171.
30. Ullmann P, Rodriguez F, Schmitz M, Meurer SK, Qureshi-Baig K, Felten P, et al. The miR-371 approximately 373 Cluster Represses Colon Cancer Initiation and Metastatic Colonization by Inhibiting the TGFBR2/ID1 Signaling Axis. Cancer Res. 2018;78(14):3793–808.
31. Han X, Li M, Xu J, Fu J, Wang X, Wang J, et al. miR-1275 targets MDK/AKT signaling to inhibit breast cancer chemoresistance by lessening the properties of cancer stem cells. Int J Biol Sci. 2023;19(1):89–103.
32. Zhou Y, Tang J, Weng M, Zhang H, Lai M. DRD4 Interacts with TGF-beta Receptors to Drive Colorectal Cancer Metastasis Independently of Dopamine Signaling Pathway. Adv Sci (Weinh). 2025;12(6):e2413953.
33. Hu C, Zhang JQ, Zhuang XY, Zhao ZD, Qian XJ, Chen Y. The hidden potential of solasonine: Targeting non-small cell lung cancer (NSCLC) metastasis through GATM and Smad2 pathways. Phytomedicine. 2025;139:156455.
34. Zhang JN, Zhang Z, Huang ZL, Guo Q, Wu ZQ, Ke C, et al. Isotoosendanin inhibits triple-negative breast cancer metastasis by reducing mitochondrial fission and lamellipodia formation regulated by the Smad2/3-GOT2-MYH9 signaling axis. Acta Pharmacol Sin. 2024;45(12):2672–83.
35. Liu Q, Liu C, Dong Y, Li H, Ren J. Circ_NNT suppresses the apoptosis and inflammation in glucose-induced human retinal pigment epithelium by regulating miR-320b/TIMP3 axis in diabetic retinopathy. Clin Immunol. 2022;238:109023.
36. Wang D, Mendoza JJ, Xiang P, Zhang Y, Tang L, Zhang J, et al. circADARB1 enhances ZEB1 expression in an m(6)A-dependent manner to promote the invasion and migration of nasopharyngeal carcinoma. Int J Biol Macromol. 2025;318(Pt 4):145187.
37. Li X, Wang C, Zhang H, Li Y, Hou D, Liu D, et al. circFNDC3B Accelerates Vasculature Formation and Metastasis in Oral Squamous Cell Carcinoma. Cancer Res. 2023;83(9):1459–75.
38. Li Y, Wang Z, Su P, Liang Y, Li Z, Zhang H, et al. circ-EIF6 encodes EIF6-224aa to promote TNBC progression via stabilizing MYH9 and activating the Wnt/beta-catenin pathway. Mol Ther. 2022;30(1):415–30.
39. Ouyang X, He Z, Fang H, Zhang H, Yin Q, Hu L et al. A protein encoded by circular ZNF609 RNA induces acute kidney injury by activating the AKT/mTOR autophagy pathway. Mol Ther. 2022;31(6):1722–38.
40. Jiang T, Xia Y, Lv J, Li B, Li Y, Wang S, et al. A novel protein encoded by circMAPK1 inhibits progression of gastric cancer by suppressing activation of MAPK signaling. Mol Cancer. 2021;20(1):66.
41. Huang J, Dong X, Gong Z, Qin LY, Yang S, Zhu YL, et al. Solution structure of the RNA recognition domain of METTL3-METTL14 N(6)-methyladenosine methyltransferase. Protein Cell. 2019;10(4):272–84.
42. Su S, Li S, Deng T, Gao M, Yin Y, Wu B et al. Cryo-EM structures of human m(6) A writer complexes. Cell Res. 2022;32(11):982–94.
43. Abdollahi S, Ardekanizadeh NH, Poorhosseini SM, Gholamalizadeh M, Roumi Z, Goodarzi MO et al. Unravelling the complex interactions between the FTO gene, lifestyle, and cancer. Adv Nutr. 2022;13(6):2406–19.
44. Shen D, Wang B, Gao Y, Zhao L, Bi Y, Zhang J, et al. Detailed resume of RNA m(6)A demethylases. Acta Pharm Sin B. 2022;12(5):2193–205.

45. Lasman L, Krupalnik V, Viukov S, Mor N, Aguilera-Castrejon A, Schneir D, et al. Context-dependent functional compensation between Ythdf m(6)A reader proteins. Genes Dev. 2020;34(19–20):1373–91.
46. Ramesh-Kumar D, Guil S. The IGF2BP family of RNA binding proteins links epitranscriptomics to cancer. Semin Cancer Biol. 2022;86(Pt 3):18–31.
47. He Q, Hao Q, Wu Y, Vadgama JV, Jiang Y. CircRAD54L2 promotes triple-negative breast cancer progression by regulating the miR-888 family/PDK1 axis. Life Sci. 2023;312:121128.
48. Wang F, Yu C, Chen L, Xu S. Landscape of circular RNAs in different types of lung cancer and an emerging role in therapeutic resistance (Review). Int J Oncol. 2023;62(2):21.
49. Razpotnik R, Vidmar R, Fonovic M, Rozman D, Rezen T. Circular RNA hsa_circ_0062682 Binds to YBX1 and promotes oncogenesis in hepatocellular carcinoma. Cancers (Basel). 2022;14(18):4524.
50. Lin X, Zhong L, Wang N, Chu X, Liu B. Hsa_circ_0103232 promotes melanoma cells proliferation and invasion via targeting miR-661/RAB3D. Cell Cycle. 2022;21(17):1811–26.
51. Hanniford D, Ulloa-Morales A, Karz A, Berzoti-Coelho MG, Moubarak RS, Sanchez-Sendra B, et al. Epigenetic Silencing of CDR1as Drives IGF2BP3-Mediated Melanoma Invasion and Metastasis. Cancer Cell. 2020;37(1):55–e7015.
52. Jiang Z, Chu PG, Woda BA, Rock KL, Liu Q, Hsieh CC, et al. Analysis of RNA-binding protein IMP3 to predict metastasis and prognosis of renal-cell carcinoma: a retrospective study. Lancet Oncol. 2006;7(7):556–64.
53. Panebianco F, Kelly LM, Liu P, Zhong S, Dacic S, Wang X, et al. THADA fusion is a mechanism of IGF2BP3 activation and IGF1R signaling in thyroid cancer. Proc Natl Acad Sci U S A. 2017;114(9):2307–12.
54. Jeng YM, Chang CC, Hu FC, Chou HY, Kao HL, Wang TH, et al. RNA-binding protein insulin-like growth factor II mRNA-binding protein 3 expression promotes tumor invasion and predicts early recurrence and poor prognosis in hepatocellular carcinoma. Hepatology. 2008;48(4):1118–27.
55. Jia M, Gut H, Chao JA. Structural basis of IMP3 RRM12 recognition of RNA. RNA. 2018;24(12):1659–66.
56. Wang P, Doxtader KA, Nam Y. Structural Basis for Cooperative Function of Mettl3 and Mettl14 Methyltransferases. Mol Cell. 2016;63(2):306–17.
57. Patil DP, Chen CK, Pickering BF, Chow A, Jackson C, Guttman M, et al. m(6)A RNA methylation promotes XIST-mediated transcriptional repression. Nature. 2016;537(7620):369–73.

## Publisher's note